Afterslip and viscoelastic relaxation following the 1999 M 7.4 İzmit earthquake from GPS measurements

L. Wang,[1,2] R. Wang,[1] F. Roth,[1] B. Enescu,[3] S. Hainzl[1] and S. Ergintav[4]

[1]*Department of Physics of the Earth, Deutsches GeoForschungsZentrum, Potsdam, Germany. E-mail: wanglf@gfz-potsdam.de*
[2]*China Earthquake Networks Center, China Earthquake Administration, Beijing, China*
[3]*Earthquake Research Department, National Research Institute for Earth Science and Disaster Prevention (NIED), Tsukuba, Japan*
[4]*TUBITAK MRC Earth and Marine Sciences Institute, Gebze, Kocaeli, Turkey*

SUMMARY

Intensive global positioning system (GPS) monitoring after the 1999 İzmit earthquake provides an opportunity to understand the postseismic behaviour of a strike-slip fault and the rheology below the brittle upper crust. Two data sets are available: displacements measured during the first 300 days after the İzmit earthquake and velocity measurements between 2003 and 2005. Using an inversion method and a forward modelling, respectively, we investigate two mechanisms: (1) afterslip on and below the coseismic rupture plane and (2) viscoelastic stress relaxation in the lower crust and upper mantle described by a Maxwell or a standard linear solid (SLS) rheology. The inversion results show that the first several months following the İzmit earthquake were dominated by afterslip at depths shallower than 30 km and the slip amount decayed with time; after that, apparent afterslip has a very different spatial distribution and is located much deeper. For viscoelastic relaxation, a model with an elastic upper crust and a Maxwell viscoelastic lower crust overlying a Maxwell mantle (E-M-M) fits the data measured in the first 300 days better in the far field than in the near field. However, the observed far-field, 300-day displacement and the long-term (2003–2005) displacement, which might be dominated by viscoelastic relaxation, cannot be described by a Maxwell rheological model with constant viscosity: the effective viscosity increases over time. Therefore, we have built a refined rheological model: an elastic upper crust and an SLS lower crust overlying a Maxwell viscoelastic mantle (E-SLS-M). Our best solution yields a viscosity for the lower crust of $\sim 2 \times 10^{18}$ Pa s, a relaxation strength of 2/3 and a viscosity for the Maxwell mantle of 7×10^{19} Pa s. Finally, we explain the data using a composite model, consisting of the preferred E-SLS-M model and the afterslip model obtained from the residual displacement after correcting for viscoelastic relaxation. For the early time period, the residual displacements can be mainly explained by a shallow afterslip whose magnitude decays with time and whose spatial distribution is stable, whereas the residual displacements for the later time period require negligible afterslip. It indicates that the postseismic deformation in the later time period induced by a deep source can be almost entirely explained by the E-SLS-M model. The composite model can generally explain the data in the entire spatial and temporal space.

Key words: Seismic cycle; Transient deformation; Elasticity and anelasticity.

1 INTRODUCTION

Many large earthquakes have been followed by postseismic deformation. Obvious changes of displacement field were observed, for example, after the 1946 M 8.2 Nankaido earthquake, Japan, (Okada & Nagata 1953) and after the 1960 M 9.5 Valdivia earthquake, Chile (Lorenzo-Martín *et al.* 2006a). Postseismic deformation, lasting days to years and covering areas with dimensions of several kilometres up to hundreds of kilometres, has been explained by af-

terslip, viscoelastic stress relaxation or poroelastic rebound. These three mechanisms are predominant in different temporal and spatial domains (Segall 2004). Poroelastic rebound occurs mostly in a short time period of months after a large earthquake and/or in a small-scale area, usually within 10–30 km from the fault (Peltzer *et al.* 1998; Jónsson *et al.* 2003; Freed *et al.* 2006), whereas afterslip and, especially, viscoelastic relaxation dominate a much larger temporal and spatial space. For example, in the case of the 1992 M 7.4 Landers earthquake, it was reported that poroelastic rebound

might contribute to the postseismic deformation (Peltzer *et al.* 1998; Fialko 2004) in a region of 10–20 km from the fault. On the other hand, it was found that this large event was followed by afterslip, with an exponential relaxation time of ∼3 months and influencing a larger area (Shen *et al.* 1994; Savage & Svarc 1997). In addition, Deng *et al.* (1998) and Pollitz *et al.* (2000) showed that a distributed lower crust and/or upper mantle viscous flow can better explain the postseismic deformation of the first 3 yr following the Landers earthquake. As other examples, Jónsson *et al.* (2003) found that the postseismic deformation of the first 1–2 months following the 2000 June 17 and 21 *M* 6.5 earthquakes in southern Iceland were mainly related to poroelastic rebound; Ryder *et al.* (2007) showed that the postseismic deformation for 4 yr following the 1997 Manyi (Tibet) earthquake can be explained by afterslip or a viscoelastic relaxation mechanism.

Since 1939, a series of large earthquakes took place sequentially along the North Anatolian Fault (NAF). The most recent one was the devastating 1999 August 17 İzmit earthquake (*M* 7.4), which was followed 87 days later by the 1999 November 12 *M* 7.2 Düzce earthquake. Global Positioning System (GPS) monitoring was active before the 1999 İzmit earthquake and was considerably intensified after the event. On the basis of the GPS measurements in the region, Hearn *et al.* (2002) studied the postseismic deformation of the first 82 days following the İzmit earthquake using the finite element method. They found that the surface deformation in this time period could be explained better by afterslip on the fault rather than by viscous shear-zone creep or poroelastic rebound. Bürgmann *et al.* (2002) reported that the afterslip during the first 87 days occurred on and below the coseismic rupture. Ergintav *et al.* (2009) used a logarithmic time function to model 7 yr of GPS measurements after the İzmit earthquake and derived afterslip in different time periods of the first 7 days, 6 months and 6 yr after the main shock, respectively. These studies focused mainly on the fault zone mechanisms, and only a simple viscoelastic model based on Newtonian rheology was tested during the investigation for rheological properties below the brittle upper crust. In contrast to previous studies, we use

the GPS data of both short term (300 days) and long term (6 yr) measured after the İzmit earthquake and focus on both viscoelastic relaxation and afterslip. We will show that the comparison between the two mechanisms provides new insight into the crustal rheology and postseismic behaviour of the strike-slip fault.

2 DATA

2.1 GPS data measured after the İzmit earthquake

Two GPS data sets measured in different time periods are available for this research: displacements measured during the first 300 days (August 1999-June 2000) after the İzmit earthquake (Ergintav *et al.* 2002) and velocity measured between 2003 and 2005 (Ergintav *et al.* 2007). Fig. 1 shows the GPS stations that recorded the two data sets, which are referred as ERG1 and ERG2, respectively. In this study, we investigate only the horizontal displacements since the vertical displacements have large measurement uncertainties, which reach ∼10 mm or even more. The GPS measurements in the NAF zone were presented in detail in many previous studies (e.g. Bürgmann *et al.* 2002; Ergintav *et al.* 2002). Therefore, we only describe briefly the data used in this study.

There are 35 ERG1 stations, 10 continuous and 25 campaign sites, located in an area with a dimension of 100×200 km^2. Most of the stations are situated close to the fault (Fig. 1). Because the *M* 7.2 Düzce earthquake (about 100 km away from the İzmit earthquake) occurred during our observation period, that is, 87 days after the İzmit event, the coseismic displacement of the Düzce earthquake is subtracted based on a coseismic slip model (Ayhan *et al.* 2001; Ergintav *et al.* 2002). The 35 corrected displacement time-series in the first 300 days were modelled by Ergintav *et al.* (2002) by superposition of a linear and an exponential component. The exponential function describes the postseismic displacement induced by the İzmit earthquake. They estimated that the postseismic displacement has an exponential relaxation time of 57 days. On the basis of their modelling, we use the displacements at 17 time points (days
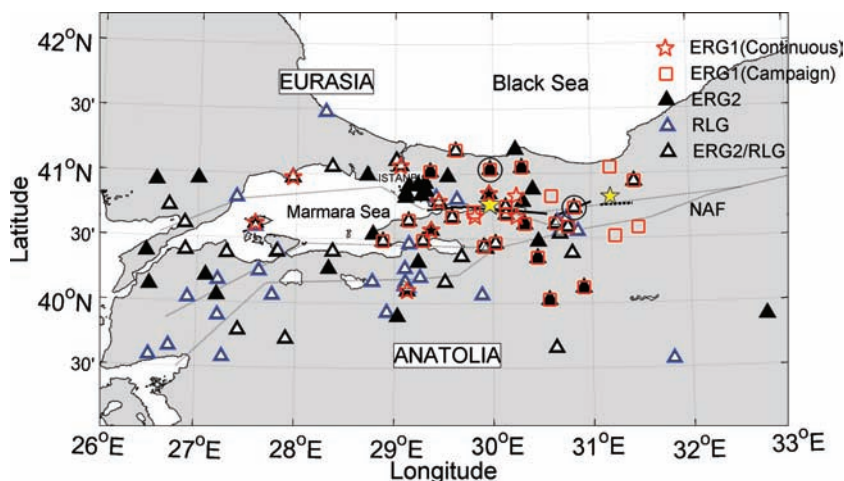

Figure 1. Map of the İzmit region showing the distribution of the GPS stations: red stars/squares mark continuous/campaign GPS sites for which data in the first 300 days after the İzmit earthquake are available (ERG1) (Ergintav *et al.* 2002); black solid triangles are GPS sites on which the velocity data measured between 2003 and 2005 was recorded (ERG2) (Ergintav *et al.* 2007); blue open triangles are GPS sites with measurements used for secular modelling (RLG) (Reilinger *et al.* 2006). Black open triangles mark GPS sites on which both ERG2 data and RLG data were recorded. Yellow stars are epicentres of the İzmit (40.76°N, 29.97°E) (Delouis *et al.* 2002) and Düzce (40.82°N, 31.20°E) (Milkereit *et al.* 2000) earthquakes; their rupture traces are shown by black bold lines (Wright *et al.* 2001) and a black dashed line (Ayhan *et al.* 2001); thin dashed lines show the simplified NAF geometry (Lorenzo-Martín *et al.* 2006b). The Anatolia block moves to the west by ∼24 mm yr^{-1} relative to the Eurasian plate. The two black circles mark the stations in which the displacements are shown as examples in Fig. 3.
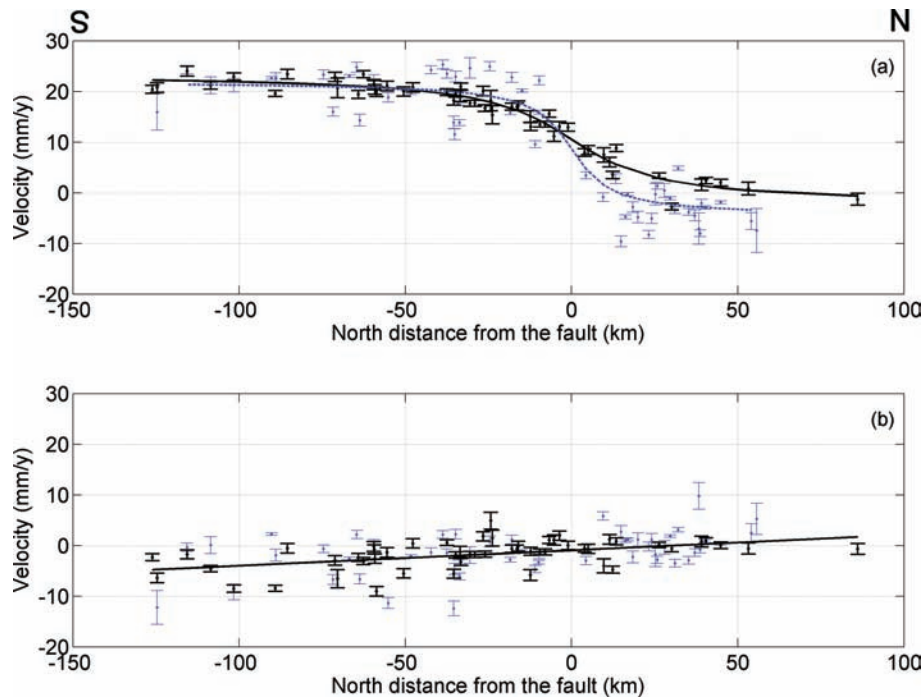
Figure 2. Velocity versus the N-S distance of the GPS site perpendicular to the fault trace along 40.72°N. The velocity value is calculated relative to the fixed Eurasian plate. (a) E-W velocity data and their measurement uncertainties at RLG (black dots with error bars) and ERG2 (blue dots with error bars) sites and their fit by eq. (1), shown as a black solid line and blue dotted line, respectively. Velocity is positive to the west. (b) N-S velocity data at RLG (black dots) and ERG2 (blue dots) stations and the linear fit to the RLG velocity data (black solid line). Velocity is positive to the north.

9, 27, 45 . . .) with an 18-day interval between 9 and 300 days after the İzmit earthquake. This data set is named as ERG1 in this text.

The 67 ERG2 GPS stations, which recorded the velocity data measured between 2003 and 2005, are shown by black filled and black open triangles in Fig. 1. The data were collected twice a year in June and October, with a total of five campaigns between June 2003 and June 2005. The velocity values plotted along a profile perpendicular to the İzmit fault trace are shown in Fig. 2. We will show below that, according to these velocity measurements, the postseismic deformation of the İzmit earthquake can still be detected 4–6 yr after the event.

2.2 Modelling secular deformation

Postseismic modelling requires separation of the deformation induced by secular tectonic motion. In general, the secular tectonic deformation can be determined from the measurements before the large earthquake. However, most of the GPS stations used for this research were installed hours or days after the İzmit event. Therefore, the secular deformation on each GPS site is estimated through a secular model based on the GPS data of Reilinger *et al.* (2006), which were recorded between 1988 and 1999 before the İzmit earthquake in our study region (see RLG GPS stations in Fig. 1).

Under the collision of the Arabian and African plates against the Eurasian and Anatolian plates, the Anatolian block moves westwards with respect to the Eurasian Plate, causing a nearly pure right-lateral, E-W striking fault, the NAF zone. Therefore, the observed E-W secular velocity can be modelled by a fundamental function, as shown in eq. (1) (Savage & Burford 1973). It describes the fault-parallel interseismic surface displacement caused by an infinitely long dislocation slipping at rate s below a locking depth d

in an elastic half-space,

$$v(x) = A - \frac{s}{\pi} \times \arctg(x/d), \tag{1}$$

where x is the distance perpendicular to the fault, measured on the surface; A refers to the velocity close to the rupture. In this study, the velocity/displacement is calculated relative to the Eurasia Plate. We assume a fault plane along 40.72°N, according to an average NAF surface trace for the region between 26°E and 33°E. Leaving d free, we estimate from the data of Reilinger *et al.* (2006): $A = 10.5 \pm 0.2$ mm yr^{-1}, $s = 26.0 \pm 1.3$ mm yr^{-1}, $d = 19.8 \pm 2.7$ km and a residual standard error of 1.5 mm yr^{-1} (black symbols, Fig. 2a). The estimated d value is close to the locking depth of $\sim$18 km in the NAF zone (Hearn *et al*. 2002; Lorenzo-Martín *et al*. 2006b). Based on the secular model, the Anatolian block in the İzmit region has an estimated westward movement relative to the Eurasian Plate of $\sim$26 mm yr^{-1}, which is close to the value of $\sim$24 mm yr^{-1} derived by McClusky *et al.* (2000) and Flerit *et al*. (2003). The N-S displacements are very small and have a weak linear trend, as shown in Fig. 2b. A linear model is considered to fit these data. Influenced by the complex geometry of the NAF (Fig. 1) in the west and south areas, the N-S displacement measurements on the south side of the rupture show a stronger scatter than the E-W ones, and the linear fit model has a relatively large standard error of 2.3 mm yr^{-1} (black symbols, Fig. 2b).

2.3 Subtraction of secular movement from the displacement data

Because RLG and ERG1/ERG2 stations (see Fig. 1) have a similar coverage in the study area, the 2-D secular model obtained based on RLG GPS data can approximate the interseismic deformation at each ERG1/ERG2 site. Therefore, the secular deformation can be
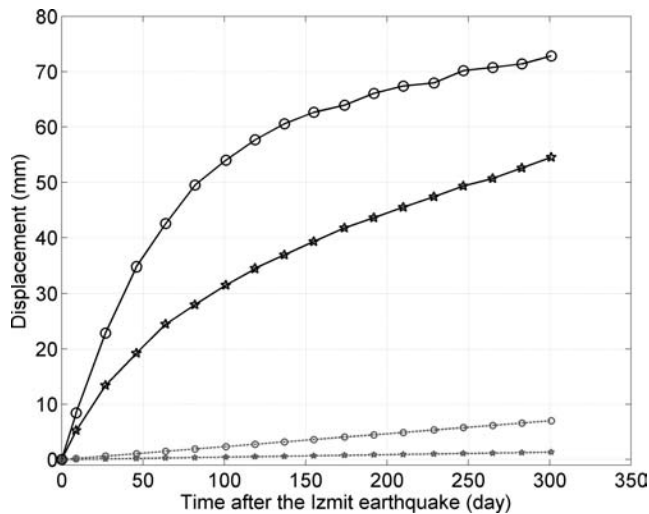
Figure 3. Calculated secular displacement (grey dotted) and secular corrected postseismic displacement (black solid) observed at two GPS sites during the first 300 days following the İzmit earthquake. The two sites (circled in Fig. 1), which are located 1.64 km and 34.81 km normal to the fault trace, are marked by circles and stars, respectively.

Figure 4. V_p, V_s and ρ profiles for the stratified medium used in this study (Milkereit *et al*. 2000). The horizontal lines mark the three layers: the upper crust (0–20 km), lower crust (20–35 km) and mantle (>35 km).

Table 1. Source parameters of the İzmit (İz) and Düzce (Dc) earthquakes (Ayhan *et al*. 2001; Wright *et al*. 2001).

Fault	Slip	Top-left corner		Length	Width	Strike	Dip	Rake
Patch	(m)	Latitude	Longitude	(km)	(km)	(°)	(°)	(°)
İz_1	1.7	40.72	29.33	20.15	20.0	84.22	88.8	174.0
İz_2	2.5	40.74	29.57	10.45	20.0	91.18	86.9	171.0
İz_3	4.9	40.75	29.69	20.34	20.0	96.20	86.9	178.0
İz_4	4.6	40.72	30.15	18.17	20.0	276.96	88.9	–178.0
İz_5	2.1	40.69	30.55	34.25	20.0	276.02	81.9	–164.8
İz_6	1.7	40.78	31.00	32.86	20.0	248.86	61.8	–168.9
Dc	3.84	40.76	31.42	28.40	17.0	268.87	51.0	–168.6

Table 1. Our study, aiming to investigate afterslip and viscoelastic relaxation mechanisms, uses a direct inversion method and a forward modelling.

3.1 Inversion for afterslip

Given the same fault geometric parameters as in the İzmit source model (Wright *et al*. 2001), the observed surface displacements are linearly related to the afterslip by

$$\mathbf{y} = \mathbf{Gb}, \tag{2}$$

where **G** is the Green function matrix, and **y** and **b** represent the data and the discrete afterslip distribution, respectively. Equation (2) is usually solved by the least-squares method using QR factorization (a decomposition of the matrix into an orthogonal and a right triangular matrix) or singular value decomposition (SVD), if it is uniquely determined or overdetermined. In many practical cases of slip inversion, however, the problem is underdetermined. In the present case, GPS measurements at fewer than 100 sites are available, whereas the number of the unknowns (slip) exceeds 1000 when we try to obtain a high resolution of the slip distribution and

---

subtracted from the GPS data measured after the İzmit earthquake. As examples, Fig. 3 shows the modelled secular displacements and observed postseismic displacements after the correction for the secular component at two ERG1 sites in the first 300 days. These postseismic displacements have magnitudes up to ~7 cm.

Concerning the precision level of the ERG1 data, the continuous and campaign GPS measurements have uncertainties (1σ) of ~2 mm and ~4 mm (Ergintav *et al*. 2002). Taking possible error due to the secular modelling into account, we assume a higher error level of the displacement data after the correction for the secular component, using 3 mm and 5 mm for the continuous and campaign measurements, respectively.

As shown in Fig. 2(a) (blue symbols), the E-W velocity measurements between 2003 and 2005 (ERG2) (Ergintav *et al*. 2007) are larger than the modelled interseismic velocity. The fit of eq. (1) to the ERG2 data (blue curve in Fig. 2a) shows a maximum difference of ~4 mm yr^{-1} from the secular model, as displayed by the black curve in the figure. After the secular component is removed, the E-W velocity data of 2003–2005 has distance-dependent values between 0.1 and 14.8 mm yr^{-1}. Most of the displacement values exceed the measurement uncertainties of ~0.90 mm yr^{-1} (Ergintav *et al*. 2007). Therefore, the displacement measured in this time period is likely to be postseismic deformation of the İzmit earthquake.

3 MODELLING METHODS

The elastic parameters used in our models are adopted from the seismic reference model for the NAF region (Milkereit *et al*. 2000) that is shown in Fig. 4. The depth of the elastic upper crust is specified as 20 km, according to the depth distribution of the relocated aftershocks of the İzmit earthquake (Milkereit *et al*. 2000). The depth of the lower crust is set as 35 km (Lorenzo-Martín, *et al*. 2006b). A coseismic slip model for the İzmit earthquake is given by Wright *et al*. (2001), derived from Synthetic Aperture Radar interferometer (InSAR) data and surface rupture. The parameters of the İzmit source model are listed in Table 1. Because we need to consider viscoelastic relaxation caused by the Düzce earthquake, its source parameters, from Ayhan *et al*. (2001), are also listed in
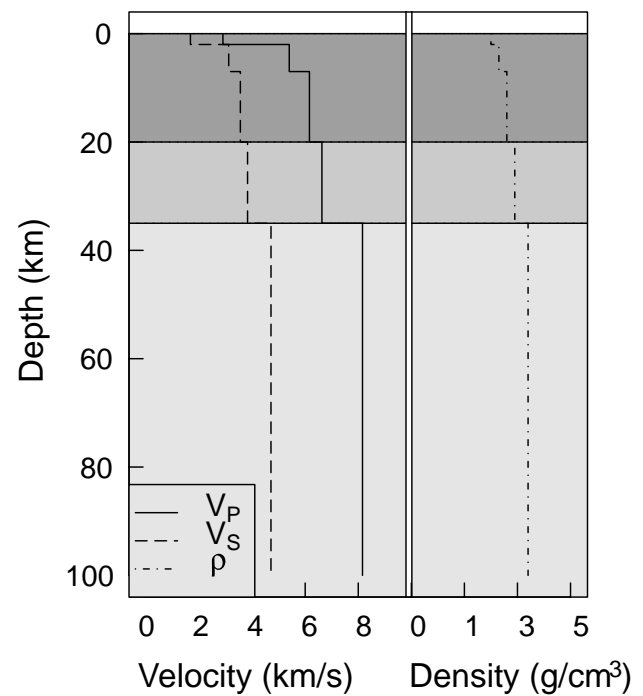
discretize the fault plane to patches of a few square kilometres. Therefore, *a priori* and/or artificial constraints are needed.

Seismological observations have shown that earthquake slip is usually characterized by one or several slip concentrations. Bouchon (1997) stated that, at large scale, the stress drop of a slip concentration is correlated with the slip magnitude. That means that the areas where large stress drop occurs also have large slip. Following the smoothing technique applied in other inversion approaches (e.g. Segall & Harris 1987), we may restrict slip models to those with an appropriate roughness in the slip or stress drop distribution. Thus, the inversion problem becomes a minimization problem applied to an objective function (in the sense of mathematical optimization) consisting of both misfit and smoothing terms. In this study, we define the objective function by

$$F(\mathbf{b}) = \|\mathbf{Gb} - \mathbf{y}\|^2 + \alpha^2 \|\mathbf{H\tau}\|^2, \qquad (3)$$

where $\boldsymbol{\tau}$ represents the shear stress drop that is linearly related to the slip distribution on the whole fault plane, $\mathbf{H}$ is the finite difference approximation of the Laplacian operator multiplied by a weighting factor proportional to the slip amplitude and α^2 is the positive smoothing factor. The weighting factor is used to better resolve slip concentrations so that they arise with clear margins such as asperities. Note that the maximum stress drop, in general, decreases with an increasing smoothing factor. Therefore, an appropriate smoothing factor can be found by matching a reasonable estimate of the maximum stress drop. In addition, because the postseismic deformation is normally consistent with the focal mechanism of the main shock, during the inversion, we constrain the rake angle of afterslip in $[\lambda - 20°, \lambda + 20°]$, where λ is the rake angle determined for the coseismic slip. A reliability test about this inversion approach, for the purpose of this study, is presented in the Appendix. A detailed explanation of technical issues will be presented in a separate paper.

3.2 Forward modelling of the viscoelastic relaxation effect

Because of the complicated relationship between the geophysical observables and the subsurface structure, a direct inversion for rheological parameters is, in general, difficult. Therefore, we use forward modelling to analyse the surface deformation caused by viscoelastic relaxation. For an isotropic elastic medium, Hooke's linear constitutive relation between the stress and the strain holds,

$$\mathbf{\Gamma} = (\lambda \nabla \cdot \mathbf{u})\mathbf{I} + \mu[\nabla \mathbf{u} + (\nabla \mathbf{u})^T], \qquad (4)$$

where $\mathbf{\Gamma}$ is the Lagrangian incremental stress tensor, $\mathbf{u}$ is the displacement vector, λ and μ are Lamé constants, $\mathbf{I}$ is the unit tensor and $(\nabla \mathbf{u})^T$ denotes the tensor transpose of $\nabla \mathbf{u}$.

According to the correspondence principle, a linear viscoelastic rheology can be implemented by a complex shear modulus in the frequency domain (Ben-Menahem & Singh 1981). We apply both the Maxwell rheology and the standard linear solid (SLS) rheology (see Fig. 5) to describe the lower crust or upper mantle. The former is a special case of the latter. Therefore, we introduce the complex shear modulus for the SLS rheology shown in Fig. 5,

$$\mu(i\omega) = \mu_2 \frac{(1 - \beta)\mu_2 + \beta i\omega\eta}{\mu_2 + \beta i\omega\eta}, \qquad (5)$$

where μ_2 is unrelaxed modulus, η is viscosity and ω is frequency. The relaxed shear modulus is $\frac{\mu_1\mu_2}{\mu_1+\mu_2}$, that is $\mu_2(1 - \beta)$, where β $(= \frac{\mu_2}{\mu_1+\mu_2})$ is the relaxation strength of an SLS body, a value between 0 and 1. When $0 < \beta < 1$, the rheological model represents the SLS rheology, whereas for the special cases of $\beta = 0$, the
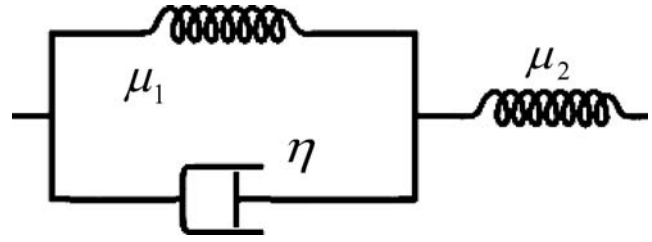

Figure 5. Schematic diagram of a standard linear solid (SLS) element. μ_2 is the unrelaxed shear modulus. The relaxed shear modulus is $\frac{\mu_1\mu_2}{\mu_1+\mu_2}$, that is, $\mu_2(1 - \beta)$, where β $(= \frac{\mu_2}{\mu_1+\mu_2})$ is the relaxation strength of an SLS body.

medium is perfectly elastic, and for $\beta = 1$, it represents the Maxwell rheology. Solving eqs (4) and (5), we can obtain the time-dependent displacement.

The forward modelling of the viscoelastic relaxation is done using the code PSGRN/PSCMP (Wang *et al.* 2006). We apply a grid search method to look for the optimal viscosities by minimizing the difference between the models and the observations, that is, the root mean square (rms) error.

4 RESULTS

4.1 Spatial afterslip distribution

It has been reported that main shock-induced afterslip might occur on the coseismic fault plane or on its extension to a deeper or shallower part of the Earth's crust (Marone & Scholz 1988; Perfettini & Avouac 2004). Therefore, we invert for afterslip on the extended fault plane down to a depth of 50 km. During the inversion, we use the fault geometry defined by Wright *et al.* (2001). The fault segments and their derived coseismic slip based on InSAR measurements are shown in the left panel of Fig. 6. We vary the rake angles around the ones determined for coseismic slip, as described in Section 3.1, and discretize the fault plane into 2×2 km^2 rectangular patches. We perform the inversions using the displacements in six time periods: the first 27 days, days 27–64, 64–101, 101–192 and 192–300 following the İzmit earthquake and between 2003 and 2005. The E-W surface displacements of the six time periods have distance-dependent values between 0.2 and 38.5 mm, 0.7 and 23.7 mm, 0.2 and 14.0 mm, 0.6 and 26.7 mm, 0.7 and 25.0 mm and 0.1 and 14.8 mm, respectively. Most of the displacements are much larger than the data uncertainty. The results are displayed in the left panel of Fig. 7. For clarity, the afterslip distributions are plotted on a vertical profile along the fault.

The inversion results show that: (1) afterslip in the first 27 days might have occurred with a maximum slip rate of ∼3 m yr^{-1}, and the most significant slip locates shallower than 30 km. (2) The slip distribution during the time periods of days 27–64 has a similar pattern as that inverted from the data in the first 27 days and displays a decaying magnitude with time. (3) Different from the first 100 days after the İzmit earthquake, the inverted slip during days 101–192 and days 192–300 is concentrated much deeper, mostly below 30 km. The slip concentration at the location between 100 and 130 km along strike might also be related to the postseismic deformation of the Düzce earthquake. (4) The inverted slip displays a gradually deep-going trend, and the time period of days 64–101 presents a transition from a shallower slip to a deeper apparent slip. (5) The inverted slip for the time period between 2003 and 2005 is much smaller than that in the time period immediately after the large earthquake and is mainly deeper than 40 km.
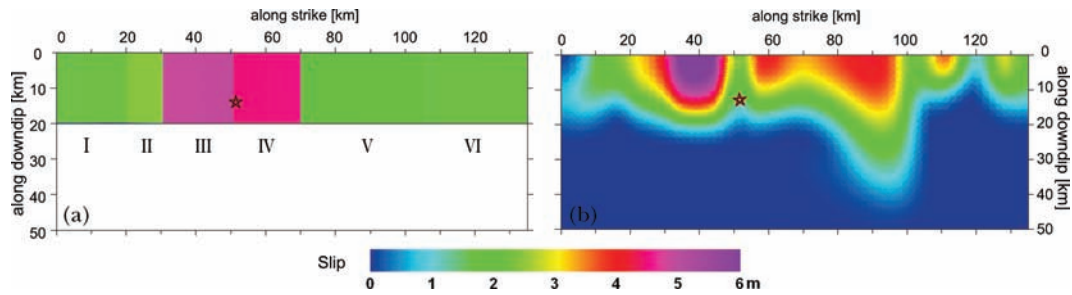
Figure 6. Two-dimensional plot showing coseismic slip of the İzmit earthquake derived by (a) Wright *et al.* (2001) and (b) our inverted coseismic slip using the GPS data of Reilinger *et al.* (2000). The red stars mark the location of the İzmit hypocentre. I–IV label the six fault segments defined by Wright *et al.* (2001).
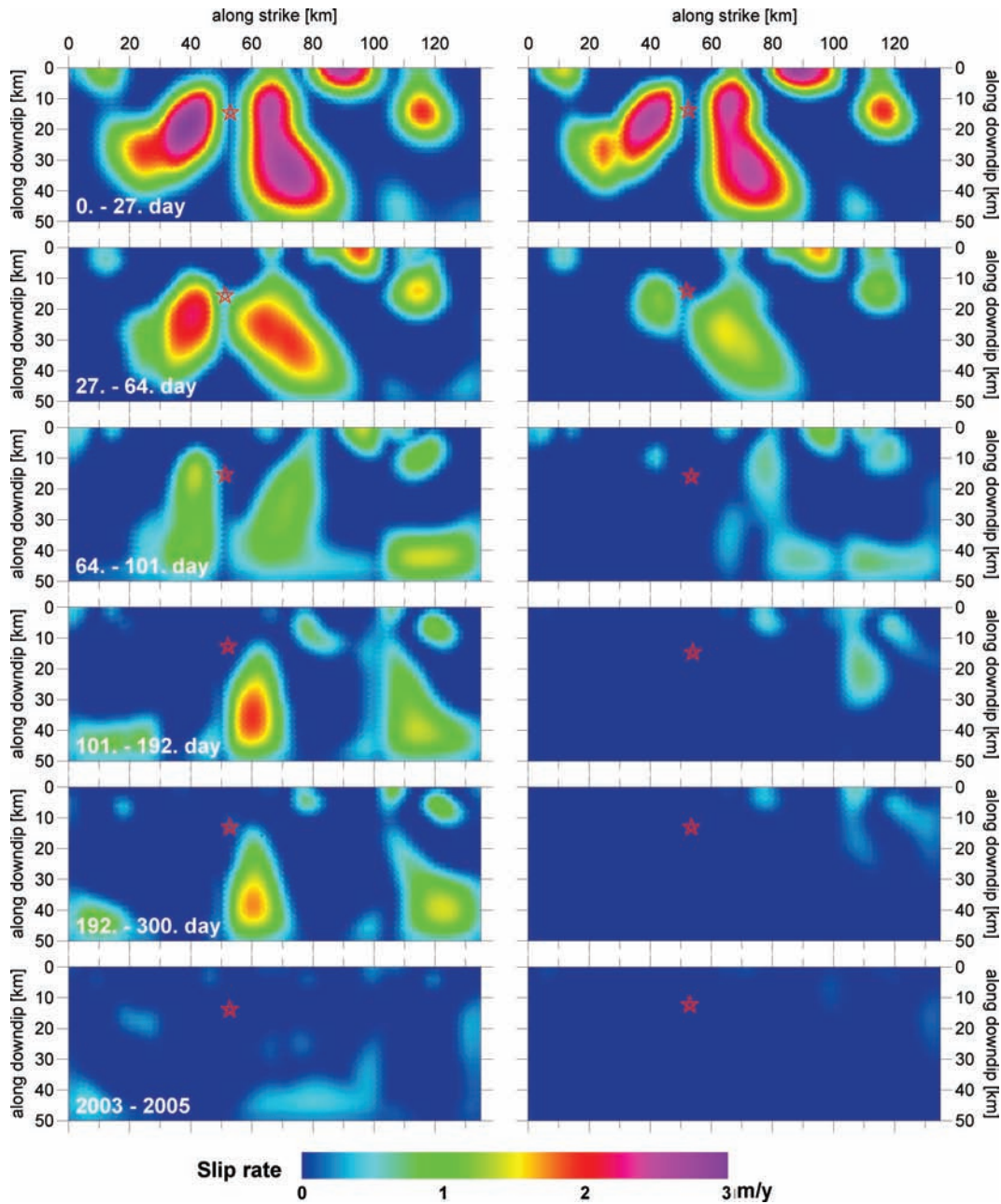

Figure 7. Two-dimensional plot showing inverted apparent slip rate along the fault plane using the postseismic GPS displacements (left panels) and the displacements after the correction for viscoelastic relaxation based on our preferred E-SLS-M model (right panels). The inversion results are for six time periods, respectively: the first 27 days, days 27–64, days 64–101, days 101–192, days 192–300 and between 2003 and 2005. The İzmit hypocentre is shown by the red stars. For the inversion, the fault plane was discretized to 2×2 km² rectangular patches.
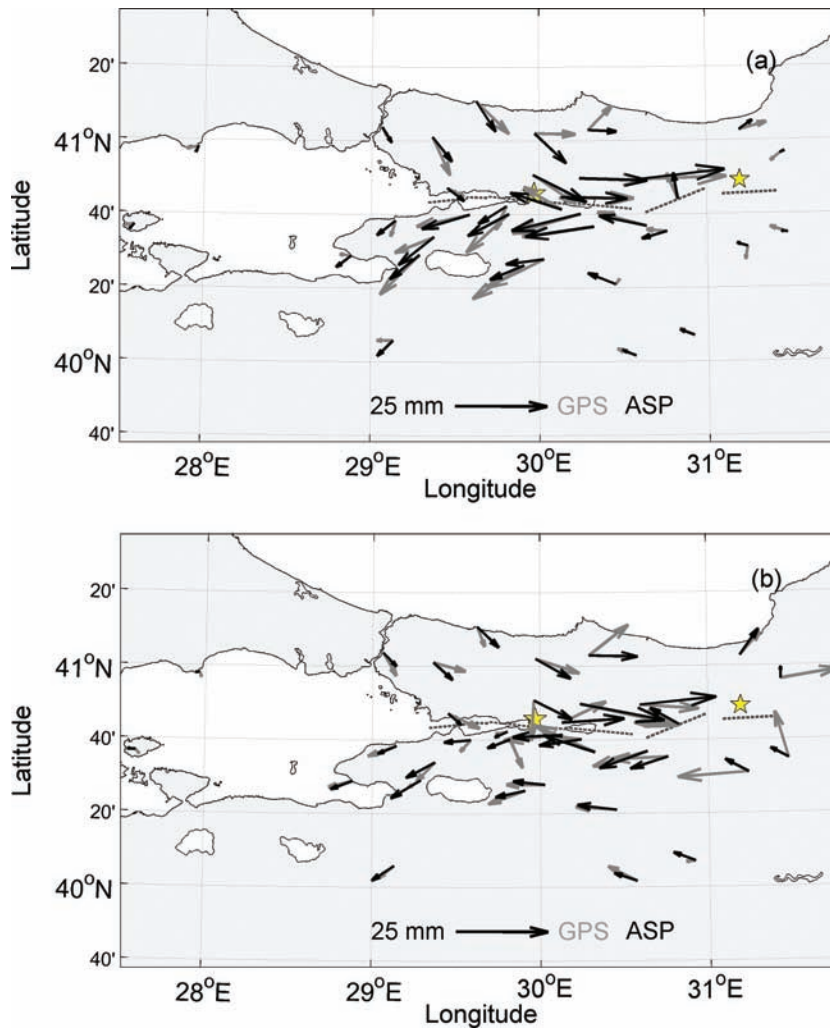
Figure 8. The observed displacements (grey arrows) and modelled displacements (black arrows) for the time period of (a) days 27–64 and (b) days 101–192 based on the afterslip (ASP) inversion results. The grey dashed lines display the fault traces of the İzmit and Düzce earthquakes and their epicentres are marked by yellow stars.

The inversion results (Table 3) indicate that the modelled displacements for the six time periods have similar fitting qualities to the data. As examples, we present in Fig. 8 the forward model for the time periods of days 27–64 and 101–192. The observed and predicted displacements are displayed by grey and black arrows, respectively. Because of the local heterogeneity, inadequacies in the model and so forth, the data on some sites cannot be fit well by the inverted slip models. The displacements at several sites around the east end of the fault, which were poorly explained by the inversion result for days 101–192, might be related to the unmodelled postseismic deformation of the Düzce earthquake.

The inversion method resolves the presumed slip on the extended coseismic fault plane, which can best reproduce the observed surface displacement. According to the inversion results, the afterslip at the shallower depth occurred in the first ∼3 months following the İzmit earthquake and the slip magnitude decayed with time. Then, the later time periods (days 100–300 and between 2003 and 2005) were governed by a deeper deformation source. As we will show in Section 5.2, according to the afterslip in the first 2 months, the decay of afterslip versus time is fast and the function used to model the afterslip decay predicts an average slip rate measured between 2003 and 2005 of ∼7 mm, much smaller than the disloca-

tion inverted (∼80 mm) from the surface displacements. Therefore, it is unlikely that the postseismic deformation measured between 2003 and 2005 was produced by the same afterslip mechanism as that in the first several months. In addition, Ergintav *et al.* (2007), using both GPS and gravity data (with the latter constraining well the vertical deformation), indicated that viscoelastic relaxation of the lower crust/upper mantle might occur between 2003 and 2005. Our inversion results also suggest that viscoelastic relaxation in the lower crust/upper mantle likely played an important role from ∼100 days after the İzmit earthquake, whereas the shallower afterslip dominated the first 2–3 months following the main shock.

4.2 Forward modelling of the viscoelastic relaxation effect based on the Maxwell rheology

Working from a simple model (with few parameters) to a more complex model, we started our viscoelastic relaxation modelling using the Maxwell rheology. We built a two-layer rheological model, made up of an elastic upper crust and a Maxwell half-space (E-M), and also a three-layer model consisting of an elastic upper crust and a Maxwell viscoelastic lower crust overlying a Maxwell viscoelastic mantle (E-M-M). The modelled elastic upper crust and lower

crust are at the depths of 0–20 km and 20–35 km, respectively (*cf*. Fig. 4). The elastic parameters of each layer are obtained from the V_p, V_s and density profiles shown in Fig. 4. We used the six-segment coseismic slip model derived by Wright *et al.* (2001) as input and calculated the effective viscosities of the inelastic layers best fitting the observations for different time periods. Our results show that the best-fit viscosity of the E-M model has a similar increasing trend with time as that of the E-M-M model (see Table 2). The best-fit viscosity of the former is in between the estimated viscosities for the lower crust and upper mantle of the latter. In comparison, the E-M-M model fits the data better than the E-M model (see Table 3) and is capable of describing more details of the medium structure. The E-M model is only a special case of the E-M-M model. Therefore, we show the detailed results based on the E-M-M model.

We estimate the viscosities using the grid search method described in Section 3.2 and apply the method to the GPS measurements in the first 300 days after the İzmit earthquake. The stability of the estimates is evaluated by the best-fit results from 500 simulations, which are obtained by adding random noise to real data within the given data uncertainties. We calculate the best-fit viscosities using the displacements measured in several time periods, days 0–27, 27–64, 64–101 and 101–300, the same as those for afterslip inversion. The viscosity estimates are presented in Table 2. The uncertainty values are specified by 25 per cent and 75 per cent quartiles of each set of 500 estimates. The misfits of the best-fit models are summarized in Table 3.

The results show that the best-fit viscosities estimated from the displacements of the first month have rather low values of $\sim 5 \times 10^{17}$ Pa s for the lower crust and upper mantle. The estimates, reflecting highly viscous flow below the brittle upper crust, are much smaller than the values obtained in previous studies (e.g. Motagh *et al.* 2007). The best-fit viscosities of the lower crust and upper mantle increase with time, and the estimates of the upper mantle viscosity are comparatively unreliable, with large uncertainties. Comparing with afterslip inversions, the rheological models with a much lower degree of freedom generally have higher misfit values (*cf*. Table 3).

Using the velocity data of 2003–2005, we estimate that the best-fit viscosities of the lower crust and upper mantle are $\sim 2 \times 10^{19}$ and 7×10^{19} Pa s, respectively. A contour plot of the rms values is shown in Fig. 9. It indicates that the viscosity estimate of the upper mantle is less constrained than that of the lower crust. However, the results suggest at least that the upper mantle has a higher viscosity than the lower crust if the surface deformation of this time period was induced only by viscoelastic relaxation. We will show in Section 5.2 that the surface deformation measured between 2003 and 2005 might be almost totally controlled by viscoelastic relaxation.

The 300-day displacements lead to the best-fit viscosities of lower crust and upper mantle far smaller than the estimates based on the velocity data of 2003–2005. The results reflect that a Maxwell rheology with constant viscosity is not sufficient to explain the GPS data over the entire time-series. For the early months after the main shock, the surface displacement might be influenced by significant afterslip at the shallower depth, as shown in the previous section.

In addition to the applied source model of Wright *et al.* (2001), we also tested the source model derived by Reilinger *et al.* (2000) to investigate the influence of different source models on viscosity estimates. Instead of a constant slip on each fault segment, the slip in Reilinger's source model varies with depth. The results (Table 2 and 3) show that the estimated viscosity for the lower crust based on the source model of Reilinger *et al.* (2000) increases with time, similar to that based on Wright's source model. The estimates based on the

Table 2. Best-fit viscosities (in Pascal seconds) of the rheological models.

	Days 0–27		Days 27–64		Days 64–101		Days 101–192		Days 192–300		2003–2005	
	η_{lc}	η_{um}	η_{lc}	η_{um}	η_{lc}	η_{um}	η_{lc}	η_{um}	η_{lc}	η_{um}	η_{lc}	η_{um}
EM[W]	$5.0\,(\pm0.2)\times10^{17}$		$1.7\,(\pm0.3)\times10^{18}$		$2.7\,(\pm0.4)\times10^{18}$		$4.2\,(\pm0.5)\times10^{18}$		$5.0\,(\pm0.8)\times10^{18}$		$3.0\,(\pm1.2)\times10^{19}$	
EM[R]	$3.0\,(\pm0.3)\times10^{17}$		$1.1\,(\pm0.2)\times10^{18}$		$1.8\,(\pm0.4)\times10^{18}$		$2.8\,(\pm0.4)\times10^{18}$		$4.1\,(\pm0.9)\times10^{18}$		$2.0\,(\pm1.0)\times10^{19}$	
EMM[W]	$5\,(\pm1)\times10^{17}$	$7\,(\pm1)\times10^{17}$	$6\,(\pm3)\times10^{18}$	$3\,(\pm5)\times10^{18}$	$4\,(\pm2)\times10^{18}$	$3\,(\pm1)\times10^{19}$	$3\,(\pm1)\times10^{18}$	$2\,(\pm4)\times10^{19}$	$2\,(\pm1)\times10^{18}$	$2\,(\pm5)\times10^{19}$	$2\,(\pm2)\times10^{19}$	$7\,(\pm7)\times10^{19}$
EMM[R]	$3\,(\pm1)\times10^{17}$	$3\,(\pm1)\times10^{17}$	$7\,(\pm1)\times10^{17}$	$3\,(\pm1)\times10^{17}$	$9\,(\pm5)\times10^{18}$	$9\,(\pm8)\times10^{18}$	$2\,(\pm2)\times10^{18}$	$6\,(\pm8)\times10^{18}$	$2\,(\pm2)\times10^{18}$	$1\,(\pm6)\times10^{21}$	$1\,(\pm2)\times10^{19}$	$9\,(\pm6)\times10^{19}$
ESM[W]	$\eta_{lc} = 2\,(\pm2)\times10^{18}$; $\eta_{um} = 7\times10^{19}$; $\beta = 2/3\,(\pm1/7)$											

Notes: η_{lc} and η_{um} refer to the viscosities of the lower crust and upper mantle, respectively. [W] refers to the source model of Wright *et al.* (2001); [R] refers to the source model of Reilinger *et al.* (2000); ASP refers to the afterslip model; EM refers to the E-M model; EMM refers to the E-M-M model; ESM refers to the E-SLS-M model.

Table 3. rms values (in millimetres) of the best-fit models.

	Days 0–27	Days 27–64	Days 64–101	Days 101–192	Days 192–300	2003–2005
ASP	6.45	3.84	2.22	5.54	8.48	4.18
EM^W	12.85	7.75	4.53	8.23	10.50	5.34
EM^R	12.90	7.83	4.60	8.75	11.78	5.40
EMM^W	12.50	7.28	4.37	8.14	10.36	4.63
EMM^R	13.53	7.49	4.41	8.62	10.68	4.68
CMP^W	6.50	4.00	2.62	6.89	9.86	4.54

Notes: CMP refers to the composite model. The other symbols have the same meaning as in Table 2.
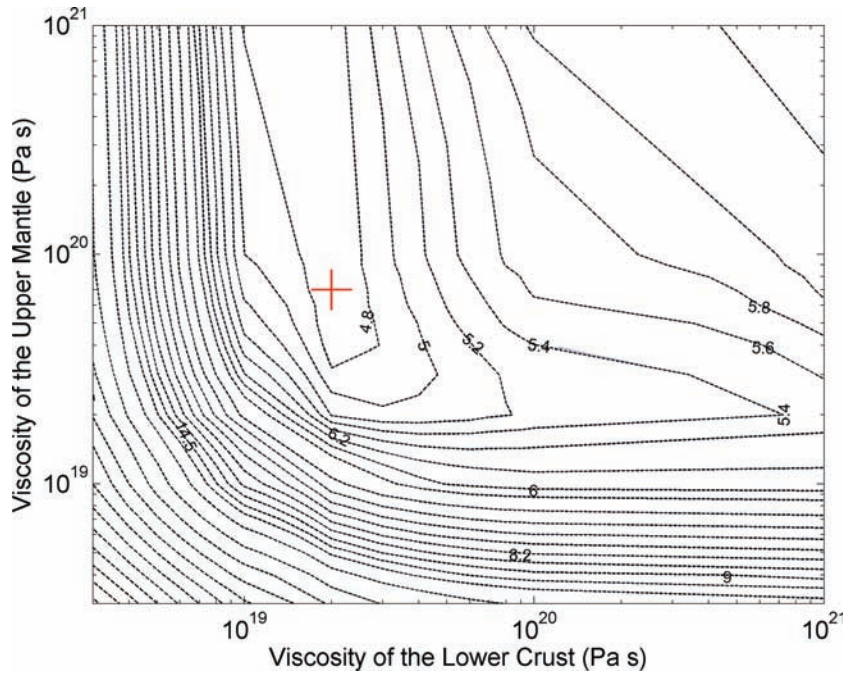

Figure 9. Misfit (rms) contour plot of the E-M-M model based on the velocity data measured between 2003 and 2005. The cross marks the location of the minimum.

former are overall smaller than those based on the latter. However, the difference between the two estimates is not significant. In this study, we stick to the simple coseismic slip model of Wright *et al.* (2001).

Compared with the afterslip mechanism, viscoelastic relaxation normally has more significant effect in the far field or on the long-term deformation (Pollitz *et al.* 2000). Therefore, to further investigate whether the E-M-M model is appropriate to explain our far-field or long-term data, we do an additional test and use two data sets: (1) the far-field (>30 km away from the fault), 300-day data to exclude significant contribution from afterslip in the near field and (2) the data measured in the long term (between 2003 and 2005). The far-field or long-term data normally have low displacement values. Therefore, we test the displacements of the first data set between different times t_1 and 300 days, for example, $D_{(9,300)}$, $D_{(27,300)}$, $D_{(46,300)}$ ..., to investigate possible variability of estimated parameters with time. During the calculation, we fix the viscosity of the upper mantle, which was less sensitive to the surface deformation of the study region, as 7×10^{19} Pa s, in agreement with our estimates of the E-M-M model based on the velocity data of 2003–2005. The results shown in Fig. 10 indicate that the viscosity estimates increase with time, which means that an E-M-M model with constants viscosities also cannot describe both the short-term, far-field deformation and the long-term deformation. Therefore, as

we will test in Section 4.4, another rheology such as the SLS is needed to describe the transient deformation.

4.3 Misfit performance of the E-M-M model in space

Relative to an afterslip model, viscoelastic relaxation has a more significant effect in the far field than in the near field. To test whether this can be seen in the data, we calculate the normalized misfit of the best-fit Maxwell rheological model on each ERG1 site,

$$\tilde{\Delta}_i = \frac{\sqrt{(D_{(i,x)} - D'_{(i,x)})^2 + (D_{(i,y)} - D'_{(i,y)})^2}}{\sqrt{D^2_{(i,x)} + D^2_{(i,y)}}}, \quad i = 1, \dots, 35. \quad (6)$$

In eq. (6), D is the observed displacement, and D' is the predicted displacement by the best-fit viscoelastic relaxation model. Small $\tilde{\Delta}$ value means that the misfit between the model and the observation is low and the model can well explain the observation.

Because the rheological models for the different time periods have similar fitting quality to the data (*cf*. Table 3), we only present in Fig. 11 the result for days 101–192 as an example. The displacements observed and predicted by the best-fit Maxwell rheological model are shown by grey and black arrows, respectively. The normalized misfit on each ERG1 site for this time period is displayed in Fig. 12. The normalized misfit $\tilde{\Delta}$ values are plotted against the
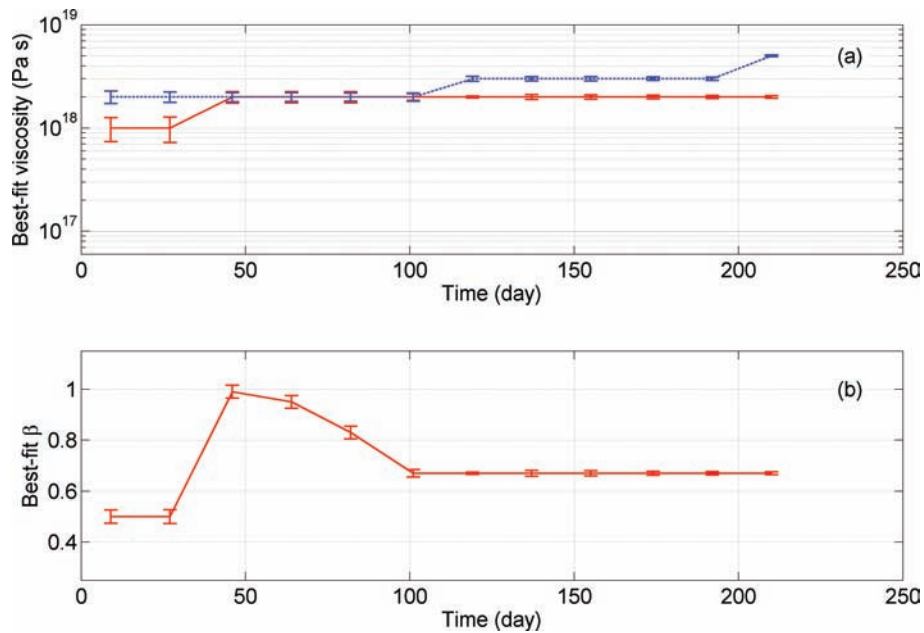
Figure 10. Grid search results for the E-M-M model and the E-SLS-M model using the far-field (>30 km from the fault) displacements between t_1 and day 300 ($D_{(t_1,300)}$, ERG1 data), together with the 2003–2005 velocity measurement. The estimates of lower crust viscosity (blue dashed line), based on the E-M-M model, with mantle viscosity of 7×10^{19} Pa s, are plotted in (a). Red lines show estimated viscosity (a) and relaxation strength (b) of the E-SLS-M model versus t_1.
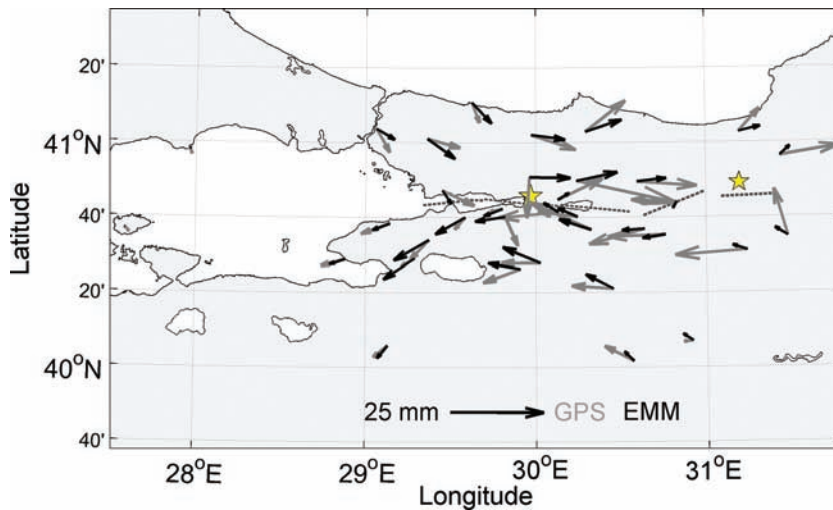

Figure 11. The observed (grey arrows) and modelled (black arrows) displacements for the time period of days 101–192 based on the best-fit E-M-M model. The grey dashed lines display the fault traces of the İzmit and Düzce earthquakes and their epicentres are marked by yellow stars.

distance of each ERG1 site perpendicular to the simplified fault trace along 40.72°N. As the İzmit rupture is nearly a pure E-W strike-slip fault, we treat the $\tilde{\Delta}$ values on the north and south sides of the fault equally and plot the absolute distance in Fig. 12. Some $\tilde{\Delta}$ values are larger than 1 (open triangles in the figure), implying that the movements do not agree with the assumed mechanism and that the data on these sites cannot be described by viscoelastic relaxation at all. Most of such large $\tilde{\Delta}$ values are on the sites near the fault. This inconsistency could relate to local heterogeneities that cannot be fully described by our coseismic slip model or reflect a comparatively poor measurement on the individual sites. When neglecting the outliers, we notice that most of the data (except one) measured about 30 km and further away from the fault can be well explained by the rheological model with normalized misfits of less

than 0.6. The spatial scale of 30 km agrees with the theoretical results obtained by Hetland & Hager (2006). They demonstrated that within several relaxation times, viscoelastic relaxation of the lower crust produces the most significant surface deformation at a distance about two times the elastic layer depth (20 km in our case) away from the fault.

4.4 Forward modelling of the viscoelastic relaxation effect based on SLS rheology

According to the results from Sections 4.2 and 4.3, a Maxwell rheological model with constant viscosity cannot describe the postseismic deformation that occurred in the far field and long term, where viscoelastic relaxation should be significant. Our result that
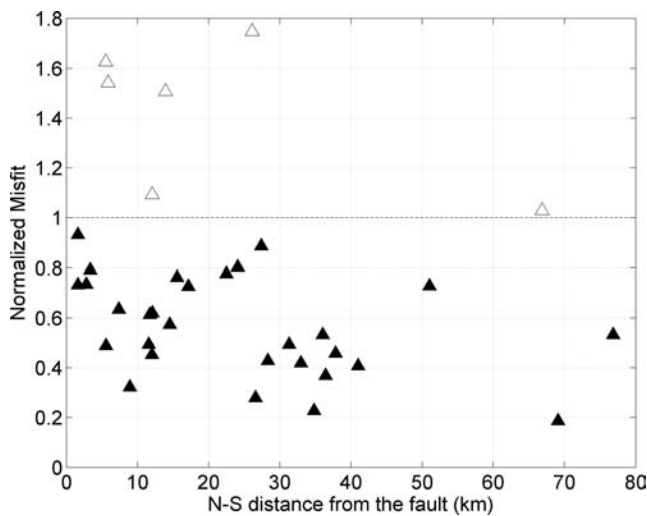
Figure 12. Normalized misfit $\tilde{\Delta}$ of the best-fit E-M-M model for the time period of days 101–192 on each EGR1 GPS site versus the N-S distance of the site perpendicular to the fault trace along 40.72°N. Some outliers have $\tilde{\Delta}$ values larger than 1.0, which implies that the data on these sites cannot be described by the viscoelastic relaxation mechanism at all, which are shown by open triangles.

the best-fit viscosity of the Maxwell rheology increases with time could be attributed to two possibilities: (1) even though the surface displacement several months after the big event was dominated by a deep viscoelastic relaxation, the shallow afterslip still contributed to the displacement field and/or (2) a Maxwell element is not appropriate for the description of the lower crust/mantle rheology, and a rheological model that can describe a transient process is necessary.

Therefore, we build a refined rheological model composed of an elastic upper crust and an SLS lower crust overlying a Maxwell viscoelastic mantle (termed as E-SLS-M). Unlike a Maxwell rheology, the SLS has a long-term elastic strength and can model a transient process. To reduce the number of model parameters, we still apply the Maxwell rheology to describe the mantle.

Using both the 300-day, far-field data (>30 km away from the fault) and the long-term data (between 2003 and 2005), we test the displacements between different times t_1 and days 300 (e.g. days 9–300, 27–300). We estimate two free parameters of the SLS element, η and μ_1, as displayed in Fig. 5, which govern the transient deforming process. To obtain μ_1, we estimate the relaxation strength $\beta = \frac{\mu_2}{\mu_2+\mu_1}$. The estimates (red lines, Fig. 10) show that after 100 days from the İzmit earthquake, the viscosity and the relaxation strength have stable values of 2×10^{18} Pa s and $\beta = 2/3$, that is, $\mu_1 = 0.5\mu_2$. The estimated SLS rheology has a relaxation time $(\frac{\eta}{\mu_1+\mu_2})$ of 1 yr. We calculate that the best-fit E-SLS-M model for the far-field data during 100–300 days and the long-term data (2003–2005) has an rms value of 4.89 mm.

If we base the E-SLS-M model only on the velocity field data of 2003–2005, the best-fit model has a viscosity of 10^{19} Pa s and $\beta = 2/3$, with an rms value of 4.61 mm. The misfit is only ∼0.02 mm smaller than that of the E-M-M model with viscosities of 2×10^{19} and 7×10^{19} Pa s for the lower crust and upper mantle, respectively, or of the E-SLS-M model with viscosities of 2×10^{18} and 7×10^{19} Pa s and $\beta= 2/3$. The small misfit difference reflects a similar long-term velocity field between the three models, and conversely, the best-fit E-SLS-M model with parameters of 2×10^{18} and 7×10^{19} Pa s and $\beta =2/3$ can similarly describe the long-term postseismic deformation as

the other two. However, it is superior to the other two models because it can describe both the long-term observations and the far-field, short-term observations. As an example, Fig. 13(a) shows the displacements observed and predicted by the preferred E-SLS-M model for the time period of days 101–192. Theoretically, we expect that the E-SLS-M model has a good fit in the far field and long term, as shown in Fig. 14(a). The displacement time-series at two sites predicted by the preferred E-SLS-M model are shown in Fig. 15. The clear difference between the postseismic displacements observed and predicted by the E-SLS-M model indicates that significant afterslip occurred in the early time period.

4.5 Composite model

The investigations above indicate that the time periods before and after the first 2–3 months were dominated by two different mechanisms, the shallower afterslip and the deeper viscoelastic relaxation, respectively.

Now, we analyse the inverted slip distribution after correcting for the postseismic surface deformation induced by viscoelastic relaxation based on the estimated E-SLS-M model. The results are shown in the right panel of Fig. 7. We find that after the correction for the viscoelastic relaxation, the apparent afterslip focuses more clearly at the shallower depth and shows a consistent spatial pattern. The slip magnitude decays with time. After ∼3 months from the main shock, the slip is negligible. It reflects that the deep source-induced surface deformation in the later time period was almost entirely removed based on the preferred viscoelastic model. It further proves that the surface deformation of the later time period can be mostly modelled by the estimated E-SLS-M model.

Therefore, we build a composite model, consisting of our preferred E-SLS-M model and the afterslip model obtained from the residual displacement after correcting for viscoelastic relaxation. The misfits of the composite model are summarized in Table 3. It shows that the composite model has rms values far smaller than the best-fit E-M-M models and is close to but not better than the pure afterslip inversions. This is because in the composite model, the far-field data are mostly explained by the viscoelastic relaxation model with only two free parameters, whereas for the pure afterslip inversion, because we permit slip to occur on an extended fault plane down to the depth of 50 km, this model has a much higher degree of freedom to explain both the near-field and the far-field data. Consistently, we present the observed and predicted surface displacements for the time period of days 101–192 as an example in Fig. 13(b). It shows that, compared with the preferred E-SLS-M model, which mostly explains the data in the far field, the composite model obviously improves the fits in the near field.

In addition, Fig. 14 shows the spatial and temporal distribution of normalized misfit (*cf*. eq. (6)) between the predictions and the observations on each GPS site during the first 300 days. The two predictions shown are based on the estimated E-SLS-M model and the composite models, respectively. The misfit on each GPS site is calculated using the displacement that occurred over 72 days, with each value spaced by 36 days (i.e. a 36-day overlapped displacement used during the calculations). The results generally indicate that the viscoelastic relaxation mechanism can better explain the measurements in the far field and long term than in the near field and short term. Some exceptions (e.g. the blue area in Fig. 14a, located at a distance of ∼50 km from the fault and ∼80 days from the İzmit earthquake) are likely to be related to additional postseismic deformation produced by the Düzce earthquake (e.g.
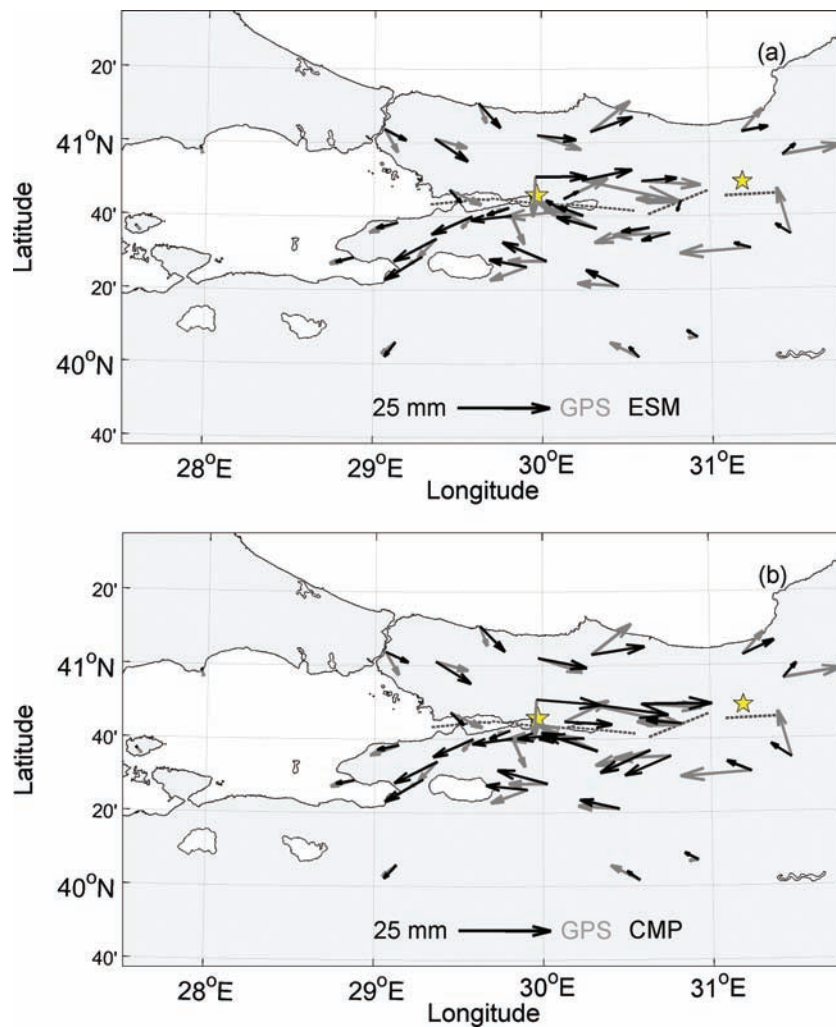
Figure 13. The displacements observed (grey arrows) and predicted (black arrows) by (a) the estimated E-SLS-M (ESM) and (b) the composite (CMP) model for the time period of days 101–192. The grey dashed lines display the fault trace of the İzmit and Düzce earthquakes and their epicentres are marked by yellow stars.

possible afterslip on the rupture plane of this large event) that is not able to be explained by the present model. Fig. 14(b) shows that, except for some areas (e.g. at a distance of 60–70 km and days 80–120) where the data can be well explained by the E-SLS-M model and the composite model produces a poorer fit prediction than the single model, the composite model, in general, explains well the postseismic displacements in both the near field and far field and the short term and long term.

5 DISCUSSION

5.1 Predominant postseismic mechanisms at different timescales

Our results indicate that the first 2 or 3 months were governed by afterslip; after that, viscoelastic relaxation played a major role. This is consistent with the results of Hearn *et al.* (2009) based on the finite element method. They found that the postseismic deformation after ∼3 months from the İzmit earthquake needs viscoelastic relaxation to explain it, whereas in the first 3 months, it is in accord with frictional afterslip on and below the İzmit earthquake rupture.

Fig. 15 shows that the contributions of viscoelastic relaxation during the first 1–2 months were very small relative to the overall surface displacement. Therefore, we neglect the effect of viscoelasticity in the first 2 months and estimate the temporal decay of afterslip. Assuming that afterslip on the fault plane follows Omori's law-type decay, the cumulative afterslip has the form (Montési 2004),

$$S(t) = c_1 \ln \left(1 + \frac{t}{c_2} \right), \tag{7}$$

where c_1 and c_2 are constants. Normalizing the inverted afterslip on each patch in the first ∼2 months to a value between 0 (when $t = 0$ day, the day of the main shock) and 1 (when $t = 64$ days), eq. (7) has the following parameter values: $c_1 = 0.33 \pm 0.01$ day and $c_2 = 3.47 \pm 0.06$ day, with a residual sum square of 6.10 (the red curve in Fig. 16a). The afterslip decay is similar to the aftershock decay. To demonstrate this, we analyse the aftershock catalogue of the Kandilli Observatory and Earthquake Research Institute (Istanbul, Turkey), with a completeness magnitude of ∼2.5 (Daniel *et al*. 2006). The result is shown by the black dotted curve in Fig. 16(a). This consistency might reflect the decay behaviour of the common stress field that governs the occurrences of both the aftershocks and the afterslip.
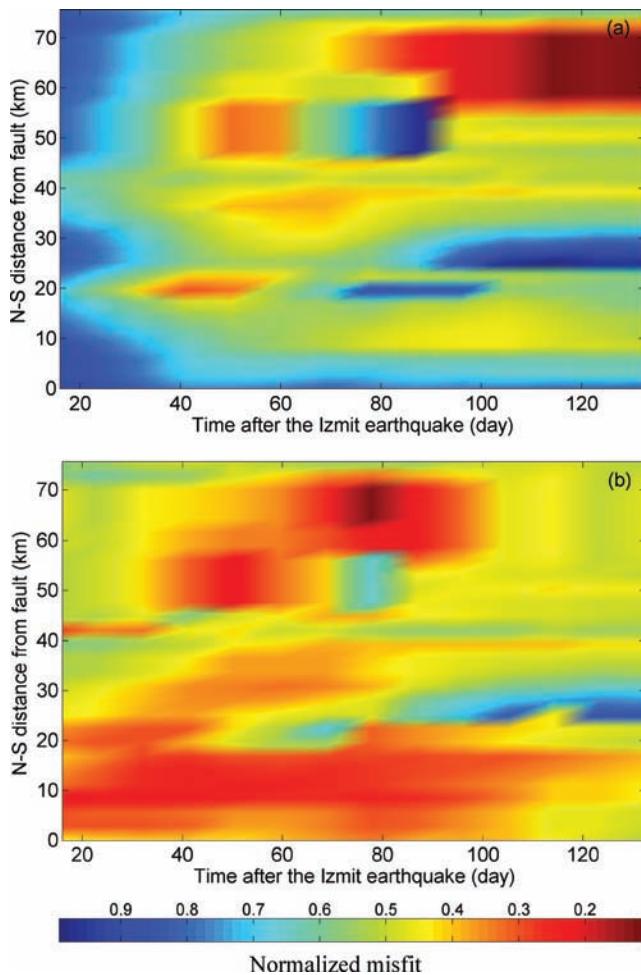
Figure 14. Temporal and spatial distribution of the normalized misfit between the displacement observed in the first 300 days and predicted by (a) E-SLS-M model with parameters $2 \times 10^{18}/7 \times 10^{19}$ Pa s and $\beta = 2/3$ and by (b) the composite model. The misfit value on each ERG1 GPS site is calculated using the displacement that occurred over 72 days, with each value spaced by 36 days (i.e. a 36-day overlapping displacement was used during the calculations).

Based on the afterslip decay function, the slip rate during the time period of days 100–300 is about 11.2 per cent of that during the first 64 days following the İzmit earthquake. Meanwhile, we estimate the average slip rate measured between 2003 and 2005 to be ~7 mm, which is far smaller than the inverted apparent slip of ~80 mm presented in Fig. 7. This result confirms that the time period between 2003 and 2005 was controlled by a different postseismic mechanism, for example, viscoelastic relaxation below the upper crust, as we studied in this work. Alternatively, deep afterslip could have taken place because of a localized deformation induced by the coseismic stress change in the discrete shear zone (Kenner & Segall 2003).

To investigate the latter case, we calculate the coseismic shear stress change downdip of the fault plane. Because the simple six-segment source model of Wright *et al*. (2001) causes strong stress singularity at the edge of the rupture plane, we use the source models of Reilinger *et al*. (2000). The results (Fig. 17) show that the locations of the high shear stress changes above the depth of 30 km are close to the location of significant afterslip along strike in

the first ~3 months. Another slightly higher shear stress change is located at the depth of ~36 km and ~50 km along strike. The location is basically consistent with the inverted apparent slip (Fig. 7, left panel) for the later time period (after the first 3 months) and the inverted results based on the synthetic data for viscoelastic relaxation (*cf*. Figs A1b and d in the Appendix). However, the possible deep afterslip does not display, as expected, a monotonic decay with time; that is, the inversion results do not show a similar deep afterslip in the first 3 months. In contrast, after correction for viscoelastic relaxation, our inverted afterslip (Fig. 7, right panel) shows a generally decaying magnitude with time. Therefore, using our preferred E-SLS-M model with only two free parameters, we can explain both the far-field and the long-term postseismic deformation, including that 4–6 yr after the İzmit earthquake. Therefore, we conclude that viscoelastic relaxation is more likely the major mechanism for the postseismic deformation after the first 3 months following the İzmit earthquake.

5.2 Rheology of the lower crust and upper mantle in the İzmit region

In this study, we use an E-SLS-M model to approximate the rheology in the İzmit region. The Maxwell rheology has commonly been used in previous investigations to describe the long-term rheological behaviour of the lower crust and upper mantle (Rundle & Jackson 1977; Savage & Prescott 1978; Hetland & Hager 2006). However, it cannot account for a rapid transient deformation. A Burgers body, composed of a Maxwell body in series with a Kelvin body, was proposed in some studies (Pollitz 2003, 2005; Hetland & Hager 2006) to model the postseismic deformation. Being able to describe a transient deforming process after a stress disturbance and behaving viscously like a Maxwell body in the long term, a Burgers rheology is a good alternative for the description of the upper mantle. However, it involves additional free parameters, which cannot be properly constrained by the limited data. In addition to the linear rheology, Freed & Bürgmann (2004) reported that a stress- or time-dependent power-law viscoelasticity of the upper mantle could explain the postseismic deformation of the 1992 Landers earthquake and the 1999 Hector Mine earthquake. However, the very different spatial distributions of the apparent slip before and after ~100 days (the left panel of Fig. 7) suggest a variation of the dominant postseismic mechanism at this time. In addition, the non-linear rheological model with more free parameters can only be performed using numerical approaches such as the finite element method. Therefore, we apply a linear rheological model, made up of an elastic upper crust, SLS lower crust and the Maxwell mantle. This model, involving only two free parameters, can describe both the transient deformation and the steady-state situation. Assuming a Maxwell material for the mantle and its viscosity of 7×10^{19} Pa s, in agreement with the best-fit estimates of the E-M-M model based on the long-term observations, we find that an SLS body with a viscosity of 2×10^{18} Pa s and a relaxation strength of 2/3 can best fit the data.

Although some studies (e.g. Pollitz 2005) reported a stronger lower crust and a weaker mantle, our results suggest that the lower crust has a lower viscosity than the upper mantle, in agreement with the results of some other investigations of postseismic deformation following large earthquakes (e.g. the 1999 Chi-Chi earthquake; *cf*. Sheu & Shieh 2004). This result (i.e. a weaker lower crust and a stronger upper mantle) is also consistent with the general view of the continental lithosphere, derived from the correlation
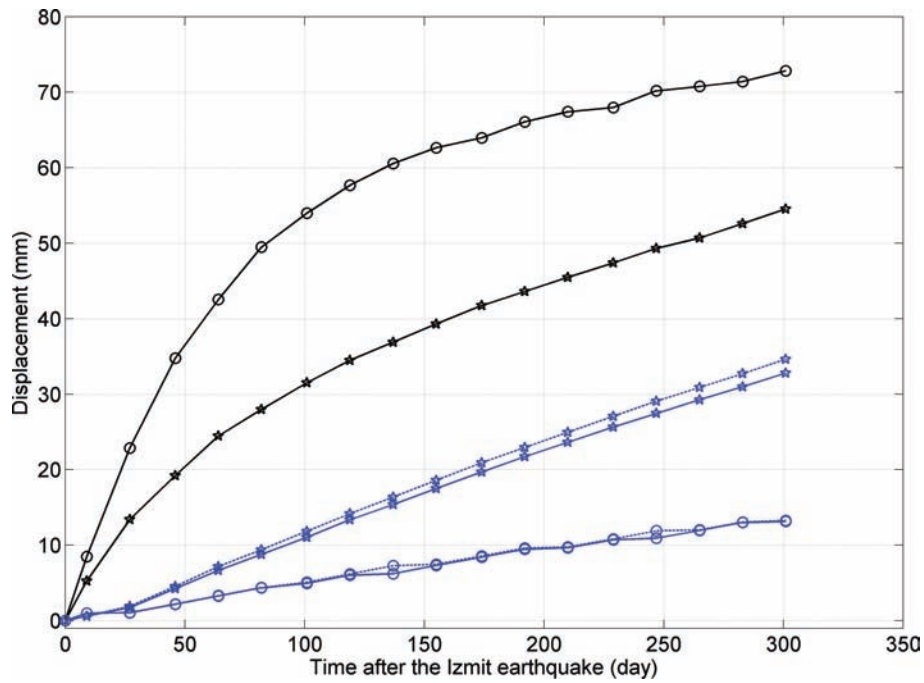
Figure 15. The observed postseismic displacements at two GPS sites (1.64 km and 34.81 km away from the fault) during the first 300 days following the İzmit earthquake are shown by two curves with black circles and black stars, respectively. The blue ones show the corresponding surface displacements at the two sites predicted by the E-SLS-M model with viscosities of 2×10^{18} and 7×10^{19} Pa s and $\beta = 2/3$, based on the stratified medium shown in Fig. 4 (solid blue lines) and a modified medium by a 50 per cent decrease of the bulk modulus (dotted blue lines). The clear difference between the postseismic displacements observed and predicted by the E-SLS-M model indicates that significant afterslip took place in the early time period.
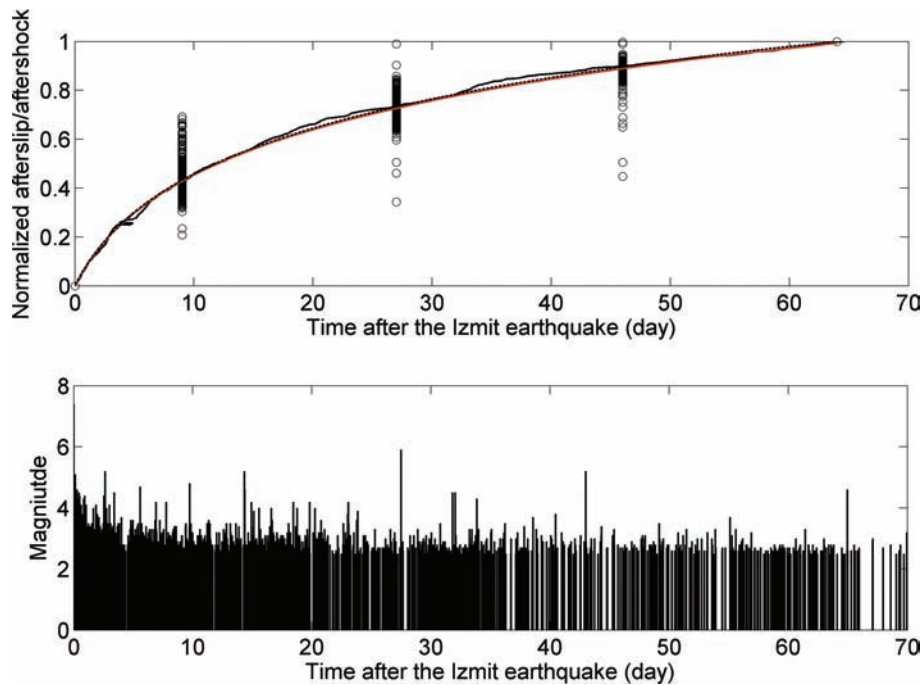

Figure 16. Omori's law decays of afterslip and aftershocks following the İzmit earthquake. (a) The normalized afterslip on each subfault (black circles) at days 0, 9, 27, 46 and 64, the normalized cumulative number of aftershocks ($M \geq 2.5$, black curve) and the fitting curve to afterslip (red curve) and the number of aftershocks (black dotted curve) by the integrated form of Omori's law (eq. 7). The normalized afterslip and aftershock number have values between 0 (at 0 day) and 1 (at 64 day). (b) M-t plot of the aftershock sequence ($M \geq 2.5$).

between the cut-off depth of continental seismicity, the onset of thermally activated processes in crustal material (Sibson 1982) and the seismic/geological evidence for a weak lower crust (Kay & Kay 1981; Kusznir 1991; Brocher *et al*. 1994).

Some uncertainties in our analysis could lead to an underestimation of the viscosity of the SLS lower crust. Although the far-field (>30 km) deformation of the first 300 days was probably dominated by viscoelastic relaxation, it still involves a small unaccounted
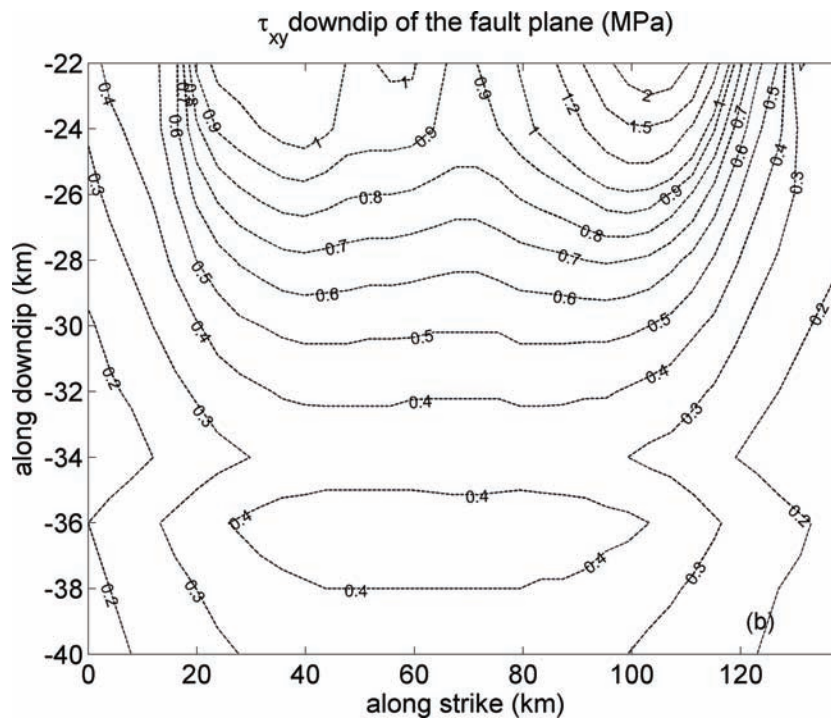
Figure 17. Shear stress change downdip of the coseismic rupture plane produced by the source model of Reilinger *et al.* (2000).

contribution of afterslip on the fault, which can cause an underestimation of the viscosity. On the other hand, our assumption of a Maxwell mantle rheology, which does not take possible transient deformation into account, could also lead to an underestimation of viscosity in the lower crust. However, the stability of our estimates over all observation periods indicates that neither bias is significant with respect to the data (the long-term deformation and the far-field, short-term deformation) used to estimate the E-SLS-M model parameters.

Some studies based on rock experiments reported that there could be a large difference between the static and the dynamic bulk modulus because of systematic differences in the deformation process or because of cracks (e.g. Cheng & Johnston 1981; Mockovciakova & Pandula 2003). Therefore, we test the viscoelastic relaxation using a different stratified medium modified by a 50 per cent decrease of the bulk modulus. The results (Fig. 15) show that this correction produces only little change in the surface deformation. In summary, we find that our E-SLS-M model with viscosities of 2×10^{18} and 7×10^{19} Pa s and $\beta = 2/3$ can represent the rheology of the İzmit region at a timescale of months to several years.

On the basis of a Maxwell half-space, Hearn *et al.* (2009) suggested that the viscosity in the region has a value of $2–5 \times 10^{19}$ Pa s, which is between the transient viscosity in the lower crust and the steady-state viscosity in the upper mantle of our E-SLS-M model; Motagh *et al.* (2007) used interseismic InSAR data to obtain a steady-state viscosity of $1.3 \times 10^{19}–3.6 \times 10^{20}$ Pa s, which is comparable with our mantle viscosity of $\sim7 \times 10^{19}$ Pa s, when the SLS lower crust behaves elastically in the long term. A similar result based on the SLS rheology was obtained by Ryder *et al.* (2007). Their model, consisting of an elastic layer and an SLS half-space with a viscosity of 4×10^{18} Pa s and $\beta = 0.68$, best explains the 4-yr postseismic displacements following the 1997 *M* 7.6 Manyi (Tibet) earthquake.

5.3 Relations between coseismic slip, afterslip and aftershocks

Fig. 6(b) shows our inverted coseismic slip of the İzmit earthquake using the GPS data of Reilinger *et al.* (2000). As for the afterslip inversion, we use an extended fault plane (Wright *et al.* 2001) down to a depth of 50 km and discretize the fault plane into 2×2 km^2 rectangular patches. Consistent with the thickness of the elastic upper crust, the inverted coseismic slip is confined well above this depth. Fig. 6 shows that the slip amount and location of our inverted maximum coseismic slip are close to those of Wright *et al.* (2001). Our slip distribution is also consistent with the coseismic slip derived by Reilinger *et al.* (2000).

In comparison, the inverted major afterslip (Fig. 7) on segments III (30–50 km along strike), IV (50–70 km along strike) and VI (~110–130 km along strike) took place in regions near or downdip of large coseismic slip (Fig. 6b). Afterslip inversions of the 1999 Chi-Chi earthquake (Hsu *et al.* 2002) and the 2003 *M* 8 Tokachi-oki earthquake (Miyazaki *et al.* 2004) demonstrate similarly that the afterslip tends to occur adjacent to areas with large coseismic slip. It suggests that stress changes caused by coseismic slip promote the afterslip. The result is consistent with the concept of velocity-strengthening frictional afterslip based on the rate-and-state friction law, which may occur on the earthquake rupture surface in areas of low coseismic slip, where the fault zone was loaded during the earthquake (Marone *et al.* 1991). Our inverted afterslip concentrations between 30 and 70 km along strike are similar to those of Bürgmann *et al.* (2002) for the first 80 days, but the slip heterogeneity is highlighted in our inversion; the slip concentration between 100 and 140 km along strike in Bürgmann *et al.* (2002) was not detected in our inversion, possibly because of our poorer data coverage in this area.
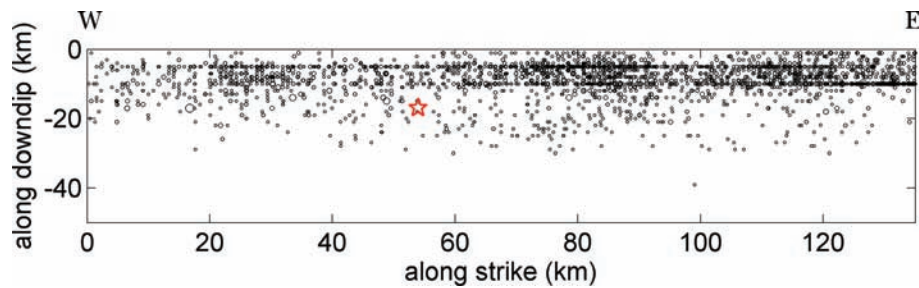
Figure 18. Two-dimensional plot of aftershocks of the İzmit earthquake that were managed by the Kandilli Observatory and Earthquake Research Institute (Istanbul, Turkey). The aftershocks ($M \geq 2.5$) in the first 64 days following the İzmit event are plotted along the fault plane. The hypocentre of the İzmit earthquake is shown by a red star.

Fig. 18 shows the spatial distribution of the aftershocks ($M \geq 2.5$) in the first 2 months following the İzmit earthquake. Many aftershocks were concentrated from ~70 to 130 km along strike (Aktar *et al.* 2004). Comparing Figs 7 and 18, we find that afterslip and aftershocks are not positively correlated. They seem to be negatively correlated in space, which means that most aftershocks occurred in the area with low afterslip.

6 CONCLUSION

We used the GPS data recorded in the first 300 days following the İzmit earthquake and 4–6 yr after the event to analyse the postseismic deformation induced by the strike-slip rupture. The comprehensive investigation of two postseismic mechanisms, afterslip and viscoelastic stress relaxation, provides an insight into the behaviour of the fault zone and the viscoelasticity below the brittle upper crust after a large earthquake. The inversion results show that the postseismic deformation in the first 2 or 3 months was dominated by afterslip at the shallower depth. The magnitude of afterslip decayed with time. In the later time period, the inverted apparent slip locates deeper and has a slip pattern very different from that in the first 2–3 months, which reflects the increasing effect due to viscoelastic relaxation in the lower crust/upper mantle.

Using both the long-term observations (between 2003 and 2005) and the far-field, short-term (the first 300 days) observations, we found that the viscosities of the best-fit Maxwell rheological model have an increasing trend with time. Therefore, we built a refined rheological model (E-SLS-M), made up of an elastic upper crust and an SLS lower crust overlying a Maxwell upper mantle. We estimated viscosities of 2×10^{18} and 7×10^{19} Pa s for the lower crust and upper mantle, respectively, and a relaxation strength $\beta = 2/3$. The best-fit rheological model can better explain the surface displacement in the far field and long term than in the near field and short term. Finally, we explained all data using the estimated E-SLS-M model together with the afterslip model obtained from the residual displacement after correcting for viscoelastic relaxation. The composite model can generally explain the data in the entire temporal and spatial space.

ACKNOWLEDGMENTS

REFERENCES

Aktar, M., *et al.*, 2004. Spatial variation of aftershock activity across the rupture zone of the 17 August 1999 İzmit earthquake, *Turkey Tectonophys.,* **391**(1–4), 325–334.

Ayhan, E., Bürgmann, R., McClusky, S., Lenk, O., Aktug, B., Herece, E. & Reilinger, R.E., 2001. Kinematics of the Mw7.2, 12 November 1999, Düzce, Turkey Earthquake, *Geophys. Res. Lett.,* **28**(2), 367–370.

Ben-Menahem, A. & Singh, S.J., 1981. *Seismic Waves and Sources,* Springer-Verlag, New York.

Bouchon, M., 1997. The state of stress on some faults of the San Andreas system as inferred from near-field strong motion data, *J. Geophys. Res.*, **102**(B6), 11, 731–811, 744.

Brocher, T.M., McCarthy, J., Hart, P.E., Holbrook, W.S., Furlong, K.P., McEvilly, T.V., Hole, J.A. & Klemperer, S.L., 1994. Seismic evidence for a lower-crustal detachment beneath San Francisco Bay, *Calif. Sci.,* **265**(5177), 1436–1439.

Bürgmann, R., Ergintav, S., Segall, P., Hearn, E.H., McClusky, S., Reilinger, R.E., Woith, H. & Zschau, J., 2002. Time-dependent distributed afterslip on and deep below the İzmit earthquake rupture, *Bull. Seism. Soc. Am.,* **92**(1), 126–137.

Cheng, C.H. & Johnston, D.H., 1981. Dynamic and static moduli, *Geophys. Res. Lett.,* **8**(1), 39–42.

Daniel, G., Marsan, D. & Bouchon, M., 2006. Perturbation of the İzmit earthquake aftershock decaying activity following the 1999 Mw 7.2 Düzce, Turkey, earthquake, *J. Geophys. Res.,* **111**, B05310, doi:10.1029/2005JB003978.

Delouis, B., Giardini, D., Lundgren, P. & Salichon, J., 2002. Joint inversion of INSAR, GPS, teleseismic and strong-motion data for the spatial and temporal distribution of earthquake slip: application to the 1999 İzmit mainshock, *Bull. Seism. Soc. Am.,* **92**(1), 278–299.

Deng, J., Gurnis, M., Kanamori, H. & Hauksson, E., 1998. Viscoelastic flow in the lower crust after the 1992 Landers, California, earthquake, *Science,* **282**(5394), 1689–1692.

Ergintav, S., Bürgmann, R., McClusky, S., Çakmak, R., Reilinger, R.E., Lenk, O., Barka, A. & Özener, H., 2002. Postseismic deformation near the İzmit earthquake (17 August 1999, M7.5) rupture zone, *Bull. Seism. Soc. Am.,* **92**(1), 194–207.

Ergintav, S., Dogan, U., Gerstenecker, C., Akmak, R.C., Belgen, A., Demirel, H., Aydın, C. & Reilinger, R.E., 2007. A snapshot (2003–2005) of the 3D postseismic deformation for the 1999, Mw = 7.4 İzmit earthquake in the Marmara Region, Turkey, by first results of joint gravity and GPS monitoring, *J. Geodyn.,* **44**(1–2), 1–18.

Ergintav, S., *et al.*, 2009. Seven years of postseismic deformation following the 1999, M = 7.4, and M = 7.2, İzmit-Düzce, Turkey earthquake sequence, *J. Geophys. Res.,* doi:10.1029/2008JB006021 (in press).

Fialko, Y., 2004. Evidence of fluid-filled upper crust from observations of postseismic deformation due to the 1992 M_w7.3 Landers earthquake, *J. Geophys. Res.,* **109**, B08401, doi:10.1029/2004JB002985.

Flerit, F., Armijo, R., King, G., Meyer, B., & Barka, A., 2003. Slip partitioning in the Sea of Marmara pull-apart determined from GPS velocity vectors. *Geophys. J. Int.,* **154**(1), 1–7.

Freed, A.W. & Bürgmann, R., 2004. Evidence of power-law flow in the Mojave desert mantle, *Nature,* **430**(6999), 548–551.

Freed, A.M., Bürgmann, R., Calais, E., Freymueller, J. & Hreinsdóttir, S., 2006. Implications of deformation following the 2002 Denali, Alaska, earthquake for postseismic relaxation processes and lithospheric rheology, *J. Geophys. Res.,* **111**, B01401, doi:10.1029/2005JB003894.

Hearn, E.H., Bürgmann, R. & Reilinger, R.E., 2002. Dynamics of İzmit earthquake postseismic deformation and loading of the Düzce earthquake hypocenter, *Bull. Seism. Soc. Am.,* **92**(1), 172–193.

Hearn, E.H., Ergintav, S., Reilinger, R.E. & McClusky, S., 2009. İzmit earthquake postseismic deformation and dynamics of the North Anatolian Fault Zone, *J. Geophys. Res.,* in press, doi:10.1029/2008JB006026.

Hetland, E.A. & Hager, B.H., 2006. The effects of rheological layering on post-seismic deformation, *Geophys. J. Int.,* **166**(1), 277–292.

Hsu, Y.J., Bechor, N., Segall, P., Yu, S.B. & Kuo, L.C., 2002. Rapid afterslip following the 1999 Chi-Chi, Taiwan Earthquake, *Geophys. Res. Lett.,* **29**(16), 1754, doi:10.1029/2002GL014967.

Jónsson, S., Segall, P., Pedersen, R. & Björnsson, G., 2003. Post-earthquake ground movements correlated to pore-pressure transients, *Nature,* **424**(6945), 179–183.

Kay, R.W. & Kay, S.M., 1981. The nature of the lower continental crust: Inferences from geophysics, surface geology, and crustal xenoliths, *Rev. Geophys.,* **19**(2), 271–297.

Kenner, S.J. & Segall, P., 2003. Lower crustal structure in northern California: implications from strain rate variations following the 1906 San Francisco earthquake, *J. Geophys. Res.,* **108**(B1), 2011, doi:10.1029/2001JB000189.

Kusznir, N.J., 1991. The distribution of stress with depth in the lithosphere: thermo-rheological and geodynamic constraints, in *Tectonic Stress in the Lithosphere,* pp. 95–107, eds. Whitmarsh, R.B., Bott, M.H.P., Fairhead, J.D. & Kusznir, N.J., The Royal Society, London.

Lorenzo-Martín, F., Roth, F. & Wang, R., 2006a. Inversion for rheological parameters from postseismic surface deformation associated to the 1960 Valdivia earthquake, *Chile Geophys. J. Int.,* **164**(1), 75–81, doi:10.1111/j.1365-246X.2005.02803.x.

Lorenzo-Martín, F., Wang, R. & Roth, F., 2006b. Elastic and inelastic triggering of earthquakes in the North Anatolian Fault zone, *Tectonophysics,* **424**(3–4), 271–289.

Marone, C.J. & Scholz, C.H., 1988. The depth of seismic faulting and the upper transition from stable to unstable slip regimes, *Geophys. Res. Lett.,* **15**(6), 621–624.

Marone, C.J., Scholz, C.H. & Bilham, R., 1991. On the mechanics of earthquake afterslip, *J. Geophys. Res.,* **96**(B5), 8441–8452.

McClusky, S., *et al.,* 2000. Global Positioning System constraints on plate kinematics and dynamics in the eastern Mediterranean and Caucasus, *J. Geophys. Res.,* **105**(B3), 5695–5720.

Milkereit, C., *et al.,* 2000. Preliminary aftershock analysis of the Mw = 7.4 İzmit and Mw = 7.1 Düzce earthquake in western Turkey, in *The 1999 İzmit and Düzce Earthquakes: Preliminary Results,* pp. 179–187, eds. Barka, A., Kozaci, Ö., Akyüz, S. & Altunel, A., Istanbul Technical University, Istanbul, Turkey.

Miyazaki, S., Segall, P., Fukuda, J. & Kato, T., 2004. Space time distribution of afterslip following the 2003 Tokachi-oki earthquake: implications for variations in fault zone frictional properties, *Geophys. Res. Lett.,* **31**, L06623, doi:10.1029/2003GL019410.

Mockovciakova, A. & Pandula, B., 2003. Study of the relation between the static and dynamic moduli of rocks, *Metalurgija,* **42**(1), 37–39.

Montési, L.G.J., 2004. Controls of shear zone rheology and tectonic loading on postseismic creep, *J. Geophys. Res.,* **109**, B10404, doi:10.1029/2003JB002925.

Motagh, M., Hoffmann, J., Kampes, B., Baes, M. & Zschau, J., 2007. Strain accumulation across the Gazikoy-Saros segment of the North Anatolian fault inferred from Persistent Scatter Interferometry and GPS measurements, *Earth Planet. Sci. Lett.,* **255**(3), 432–444.

Okada, A. & Nagata, T., 1953. Land deformation of the neighborhood of Muroto Point after the Nankaido great earthquake in 1946, *Bull. Earthq. Res. Inst. Tokyo Univ.,* **31**, 169–177.

Peltzer, G., Rosen, P., Rogez, F. & Hudnut, K., 1998. Poroelastic rebound along the Landers 1992 earthquake surface rupture, *J. Geophys. Res.,* **103**(B12), 30131–30145.

Perfettini, H. & Avouac, J.P., 2004. Postseismic relaxation driven by brittle creep: a possible mechanism to reconcile geodetic measurements and the decay rate of aftershocks, application to the Chi-Chi earthquake, Taiwan, *J. Geophys. Res.,* **109**, B02304, doi:10.1029/2003JB002488.

Pollitz, F.F., 2003. Transient rheology of the uppermost mantle beneath the Majave Desert, California, *Earth Planet. Sci. Lett.,* **215**(1–2), 89–104.

Pollitz, F.F., 2005. Transient rheology of the upper mantle beneath central Alaska inferred from the crustal velocity field following the 2002 Denali earthquake, *J. Geophys. Res.,* **110**, B08407, doi:10. 1029/2005JB003672.

Pollitz, F.F., Peltzer, G. & Bürgmann, R., 2000. Mobility of continental mantle: evidence from postseismic geodetic observations following the 1992 Landers earthquake, *J. Geophys. Res.,* **105**(B4), 8035–8054.

Reilinger, R.E., *et al.,* 2000. Coseismic and postseismic fault slip for the 17 August 1999, M7.5, İzmit, Turkey earthquake, *Science,* **289**(5484), 1519–1524.

Reilinger, R.E., *et al.,* 2006. GPS constraints on continental deformation in the Africa-Arabia-Eurasia continental collision zone and implications for the dynamics of plate interactions, *J. Geophys. Res.,* **111**, B05411, doi:10.1029/2005JB004051.

Ryder, I., Parsons, B., Wright, T.J. & Funning, G.J., 2007. Post-seismic motion following the 1997 Manyi (Tibet) earthquake: InSAR observations and modeling, *Geophys. J. Int.,* **169**(3), 1009–1027, doi:10.1111/j.1365-246X.2006.03312.x

Rundle, J.B. & Jackson, D.D., 1977. A three-dimensional viscoelastic model of a strike slip fault, *Geophys. J. Roy. Astr. Soc.,* **49**(3), 575–591.

Savage, J.C. & Burford, R.O., 1973. Geodetic determination of relative plate motion in central California, *J. Geophys. Res.,* **78**(5), 832–845.

Savage, J.C. & Prescott, W.H., 1978. Asthenosphere readjustment and the earthquake cycle, *J. Geophys. Res.,* **83**(87), 3369–3376.

Savage, J.D. & Svarc, J.L., 1997. Postseismic deformation associated with the 1992 Mw = 7.3 Landers earthquake, southern California, *J. Geophys. Res.,* **102**(B4), 7565–7577.

Segall, P., 2004. Postseismic deformation: different mechanisms in different times and places. *Eos 85* (Fall Meet. Suppl.), abstract G12A–01.

Segall, P. & Harris, R., 1987. Earthquake deformation cycle on the San Andreas fault near Parkfield, California, *J. Geophys. Res.,* **92**(B10), **10,** 511–610, 525.

Shen, Z.K., Jackson, D.D., Feng, Y.J., Cline, M., Kim, M., Fang, P. & Bock, Y., 1994. Postseismic deformation following the Landers earthquake, California, 28 June, 1992, *Bull. Seism. Soc. Am.,* **84**(3), 780–791.

Sheu, S.Y. & Shieh, C.F., 2004. Viscoelastic-afterslip concurrence: a possible mechanism in the early post-seismic deformation of the M-w 7.6, 1999 Chi-Chi (Taiwan) earthquake, *Geophys. J. Int.,* **159**, 1112–1124.

Sibson, R.H., 1982. Fault zone models, heat flow, and the depth distribution of earthquakes in the continental crust of the United States, *Bull. Seismol. Soc. Am.,* **72**(1), 151–163.

Wang, R., Lorenzo-Martín, F. & Roth, F., 2006. PSGRN/PSCMP—a new code for calculating co-postseismic deformations and geopotential changes based on the viscoelastic-gravitational dislocation theory, *Comput. Geosci.,* **32**(4), 527–541.

Wright, T., Fielding, E. & Parsons, B., 2001. Triggered slip: observations of the 17 August 1999 İzmit (Turkey) earthquake using radar interferometry, *Geophys. Res. Lett.,* **28**(6), 1079–1082.

APPENDIX: RELIABILITY TEST OF INVERSION METHOD

To check the afterslip inversion results, especially those obtained from small displacements measured between 2003 and 2005, we do the following test. We simulate two data sets, one related to afterslip on the fault plane and the other related to viscoelastic relaxation
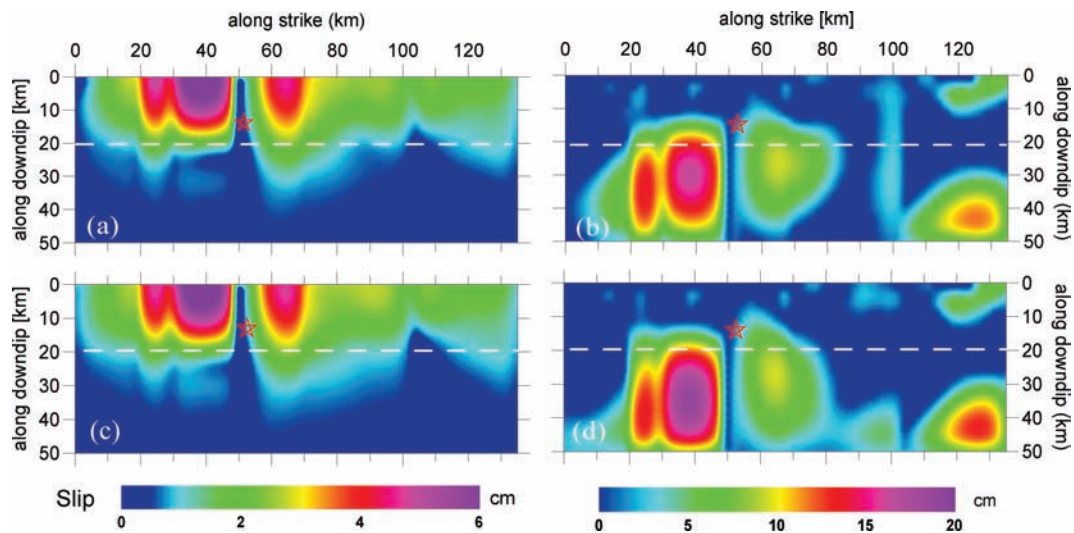
Figure A1. Inversion results from synthetic data based on afterslip (simulated by 1 per cent of coseismic slip of Wright *et al.* 2001, shown in Fig. 6a) and viscoelastic relaxation (simulated by the E-M-M model with viscosities for the lower crust and upper mantle of 2×10^{19} and 7×10^{19} Pa s, respectively), measured between 2003 and 2005 in response to the coseismic slip of the İzmit earthquake (Wright *et al.* 2001) and the Düzce earthquake (Ayhan *et al.* 2001). Inversion results from simulated data at 78 GPS sites for (a) the afterslip model and (b) the viscoelastic model. Inversion results using only part of the data (at 35 ERG1 sites) for (c) the afterslip model and (d) the viscoelastic model. The red stars mark the location of the İzmit earthquake.

below the upper crust. We first simulate the surface displacements induced by afterslip of 1 per cent of the coseismic slip derived by Wright *et al.* (2001) in an elastic, layered model. Then, we simulate the velocity field data measured between 2003 and 2005 induced by viscoelastic relaxation in response to the İzmit earthquake (Wright *et al.* 2001) and the Düzce earthquake (Ayhan *et al.* 2001) using a rheological model. This model consists of an elastic upper crust and a Maxwell viscoelastic lower crust overlying a Maxwell mantle. The viscosities of the two inelastic layers are set to 2×10^{19} and 7×10^{19} Pa s, according to our best estimates in Section 4.2. We superimpose a random component to the simulated displacement data to include the measurement uncertainty. The E-W and N-S random components are taken from two normal distributions, with standard deviations of 0.90 mm and 0.85 mm, respectively, in accord with the measurement uncertainty of the velocity data measured between 2003 and 2005 (Ergintav *et al.* 2007).

For the two simulations based on afterslip and viscoelastic relaxation, the general displacement field, in the first case, is characterized by the slip on the fault plane in the elastic layer and has a shallow slip source; in the latter case, it is characterized by a distributed deep viscous flow below the brittle upper crust. In both cases, we invert for the possible slip on the extended fault plane and test whether the inversion results reflect the deformation locations. The inversion assumes an elastic, layered medium. Note that, in the case of the non-stationary viscoelastic relaxation-induced deformation, the inversion is based on a wrong model assumption, namely an elastic rheology. The inversion result might not be able to accurately reflect the effect of the laterally distributed viscous flow, as given by viscoelastic lower crust/upper mantle. However, we will show below that the inversion can still basically resolve the depth of the deep deformation source.

The results are plotted in Fig. A1. Figs A1(a) and (b) show inversion results from the whole simulated data (for 78 GPS sites in Fig. 1), based on the afterslip and viscoelastic relaxation model, respectively. The rms values for the two inversions are 0.24 mm

and 0.25 mm. To investigate the influence of the number of data on the inversion, we use fewer data for a second set of models, namely those at the 35 ERG1 sites that recorded the displacements in the first 300 days. The results are presented in Figs A1(c) and (d), respectively. The inversions have rms values of 0.22 mm and 0.23 mm. The similarities of the inversion results based on different amount of data show that the inversion is stable.

The results also reflect the depth difference of the two modelled deformation sources, the slip in the elastic layer or the deep viscous flow. Because we used a discretized fault plane during the inversion, the obtained slip distribution for afterslip shows a smoother pattern than the input model. However, the large slip locus along strike and its depth location correspond well to the input model. The results for viscoelastic relaxation show that the resolved apparent slip concentrates below the depth of 20 km, which corresponds to the location of the assumed viscous flow source. The location of the inverted large slip along strike is consistent with the location of the high coseismic slip, where a significant stress change was produced during the earthquake.

When comparing this result with the inversion results derived from the real data shown in the left panels of Fig. 7, we find that the depth of the inverted deformation source for viscoelastic relaxation basically agrees with the apparent slip for the time period of days 100–300 and 4–6 yr after the İzmit earthquake. The apparent slip distributions east of the İzmit hypocentre shown in Figs A1(b) and (d) are similar with the apparent slip shown in the left panel of Fig. 7, whereas the significant apparent slip concentration in the west was not resolved from the real data. Note that the most significant shallow afterslip occurred west of the İzmit hypocentre in the first ∼3 months. It suggests that the stress might be relaxed mostly by afterslip in the early time period, which leads to an absence of viscoelastic relaxation-induced deformation in this area in the later time period. Therefore, a deep viscoelastic relaxation was likely the dominant mechanism after ∼100 days from the large event.